the current study with written informed consent. The NC group consisted of 15 healthy subjects (age ranging from 48 to 90 years, 66.7 ± 11.5 years (mean ± SD); eight males and seven females) without a history of central nervous system diseases or psychiatric disorders, and the AD group consisted of 15 patients (ages 55 to 85, 68.9 ± 9.6 years; four males and 11 females) diagnosed as probable AD according to the criteria of the National Institute of Neurological and Communication Disorders, Alzheimer's Disease and Related Disorders Association [16]. The study was approved by the Institutional Review Board of the National Institute of Radiological Sciences.

Radiochemical synthesis

[^{11}C]PIB was synthesized by the reaction of 2-(4′-aminophenyl)-6-hydroxy-benzothiazole and [^{11}C]methyl triflate [17]. The product had radiochemical purity greater than 95.4%. Specific activity was in the range of 56.3 to 285.3 GBq/μmol.

PET scan protocol

PET images were acquired with a Siemens ECAT EXACT HR + scanner (CTI PET systems, Inc., Knoxville, TN, USA) with an axial field of view of 155 mm, providing 63 contiguous 2.46-mm slices with 5.6-mm transaxial and 5.4-mm axial resolution. After a 10-min transmission scan for tissue attenuation correction, infusion of [^{11}C]PIB (about 370 MBq in 5 mL for 1 min) began. A PET scan in 3D mode was started after the arrival of tracer to the brain (approximately 30 s after the beginning of tracer infusion). The dynamic scans consisted of 19 frames (3 × 20 s, 3 × 40 s, 1 × 1 min, 2 × 3 min, 5 × 6 min, and 5 × 10 min) with the total scan duration of 90 min. All data processing and image reconstruction were performed using standard Siemens software, which included scatter correction, randoms, and dead time correction.

Region-of-interest delineation

Region-of-interest (ROI) analysis was performed using the PMOD software package (PMOD version 3.2; Technologies Ltd., Adliswil, Switzerland). The [^{11}C]PIB PET images were co-registered to T_1 weighted images in each subject. The following 15 ROIs were drawn manually on T_1 weighted images: frontal, mesial temporal, lateral temporal, parietal, occipital, anterior cingulate, and posterior cingulate cortices in both hemispheres as well as the reference tissue (gray matter of cerebellum). ROIs were transferred to co-registered [^{11}C]PIB PET images, and time-activity curves (TACs) were obtained in those brain regions.

Input function measurement

During PET scan, arterial blood was collected from radial artery, starting 6 s (transit delay at the blood sampling site) after the beginning of PET scan to 85 min post injection (10 × 10 s, 1 × 30 s, 9 × 2 min, 6 × 10 min, and 1 × 5 min; 27 samples). Radioactive metabolites were analyzed by a radio-thin layer chromatography (TLC) method [12], with a TLC-developing solvent (ethyl acetate/*n*-hexane = 2:1 vols). The metabolite-corrected radioactivity as well as total radioactivity in blood plasma was fitted to a mono-exponential saturation function during infusion (0 to 1 min) and the sum of three-exponential functions after the end of infusion (1 to 85 min) [12].

4P and 3P + analyses (arterial-plasma input)

Brain regional TACs were analyzed by the weighted NLS method under positive constraint of all k_i with metabolite-corrected input function to afford K_1 to k_4 estimates in 4P analysis (scan time of 90 min) and K_1 to k_3 estimates in 3P + analysis (40 min). Correction was made for blood-pool (5%) radioactivity in brain tissue [14]. Custom software operating in IDL software (version 6.0; Jicoux Datasystems, Inc., Tokyo, Japan) environment was used for the compartment model analysis.

3P++ analysis (reference tissue input)

For successful convergence in NLS optimization using Equation 1, we fixed k_{2r} to 0.178/min (mean cerebellar k_2 value by 40-min 3P + analysis; $N = 30$; SD = 0.034). Based on Equation 1 and cerebellar TAC with a fixed k_{2r} value, the time-integral of $C_r(t)$ (the second term on the right side of Equation 1) and the convolution integral (the third term) were calculated numerically without data interpolation for each scan mid-times during 0 to 40 min, and the three parameters R_1, k_2, and k_3 were estimated.

Simulation study

Generation of error-added TACs for Monte Carlo simulation

The error-free, baseline TACs (19 frames/90 min) simulating the target ROI of the NC and AD subjects were generated by using the 4P model with parameter set (K_1 = 0.180 mL/g/min, k_2 = 0.180/min, k_3 = 0.018 and 0.036/min for the NC and AD subjects, respectively, and k_4 = 0.018/min; typical values for [^{11}C]PIB) and averaged (N = 20) input function of [^{11}C]PIB. The reference ROI was the same between NC and AD subjects and was generated by using the 2P model with parameter set (K_1 = 0.180 mL/g/min, k_2 = 0.180/min) and the same input function as above. The error-added TACs for simulation were generated according to the following formula [18]:

$$\text{Error-added } C_i = C_i + \text{Rand} \times \sigma(C_i),$$
$$\sigma(C_i) = \varepsilon\sqrt{\frac{C_i}{\Delta t_i \times \exp(-\lambda t_i)}}, \quad (2)$$

where C_i is noise-free simulated radioactivity concentration at frame number i, Rand is a random number from a Gaussian distribution with a mean 0 and variance 1, ε is a

scaling factor that determines the noise level, Δt_i is scan duration of frame number i, t_i is mid-scan time of frame number i, and λ is ^{11}C decay constant. In all Monte Carlo simulations, a data set of 100 noise-added TACs was analyzed with weighted NLS, using a relative weight w_i:

$$w_i = \text{constant} \times \frac{\Delta t_i \times \exp(-\lambda t_i)}{C_i}. \quad (3)$$

Effects of PET noise on 4P, 3P+, and 3P++ analyses

Five levels of PET noise (0.025, 0.05, 0.1, 0.2, and 0.3; ε in Equation 2, relative values empirically determined) were added to the baseline TACs of the target ROI of the NC subjects. From 100 error-added TACs for each PET noise level, 100 k_3 values were estimated using 90-min 4P, 40-min 3P+, and 3P++ analyses. Coefficient-of-variation (CV) of k_3 was calculated as CV (%) = (SD/mean) × 100. In the following simulations, the PET noise was fixed at 0.1.

Effects of K_1 change in target ROI on 4P, 3P+, and 3P++ analyses

Simulated target TACs were generated by 4P model with five different K_1 values (0.12, 0.15, 0.18, 0.21, and 0.24 mL/g/min) and fixed k_3 (0.018/min) and k_4 (0.018/min). The value of K_1/k_2 was fixed at 1. The range of K_1 was determined with clinically measured K_1 for [^{11}C]PIB (0.177 ± 0.31 in NC group and 0.168 ± 0.30 in AD group; 90-min 4P analysis). Reference TAC was the same as baseline reference TAC. The k_3 bias in 90-min 4P, 40-min 3P+, and 3P++ analyses relative to the true k_3 (0.018/min) was calculated as bias (%) = (estimated k_3/true k_3 − 1) × 100.

Effects of k_2 or k_3 change in reference ROI on 3P++ analysis

In 3P++ analysis, k_{3r} was assumed to be 0 and k_{2r} was fixed as an empirical constant. The effects of k_{2r} or k_{3r} change were investigated as follows. The error-added target TACs were generated by 4P model with two different k_3 values (0.018/min for NC and 0.036/min for AD); other parameters were the same as the baseline target TAC. The error-added reference TACs were generated by 2P model with five different k_2 (0.12, 0.15, 0.18, 0.21, and 0.24/min) and fixed K_1 values (0.18 mL/g/min). Another set of simulated reference TACs was generated by 3P model (not 2P model) with five different k_3 (0, 0.002, 0.004, 0.006, and 0.008/min) and fixed K_1 (0.18 mL/g/min) and k_2 (0.18/min). The k_3 bias in 3P++ analysis was expressed relative to 3P + analysis as bias (%) = (3P++ k_3/3P + k_3 − 1) × 100.

Although k_{3r} was assumed to be 0 in Equation 1, each subject may have different k_{3r} values that deviated from 0. In simulations to investigate the effect of the individual k_{3r} variation on 3P++ analysis, we defined the k_3 value empirically corrected for nonzero k_{3r} as follows: $k_3' = k_3 + k_{3r}$, where k_3 is the k_3 estimate of target ROI by 3P++ analysis and k_{3r} is the k_3 estimate of reference ROI by 3P + analysis (true reference k_3). Bias in 3P++ k_3' relative to 3P + k_3 was compared with the bias in 3P++ k_3 to 3P + k_3.

Results

Goodness of model fits in 3P++ analysis

Figure 1A shows an example of the curve fitting of [^{11}C]PIB cerebellar TAC data to the 2P model, where a good fit is seen during 0 to 40 min after tracer injection. Figure 1B shows the fits of cerebral cortical TAC data (0 to 40 min) to the 3P + and 3P++ models. The goodness-of-fit by 3P++ model (reference tissue input) is almost indistinguishable from that by 3P + model (arterial-plasma input). Kinetic parameters (K_1 = 0.161 mL/g/min, k_2 = 0.167/min and

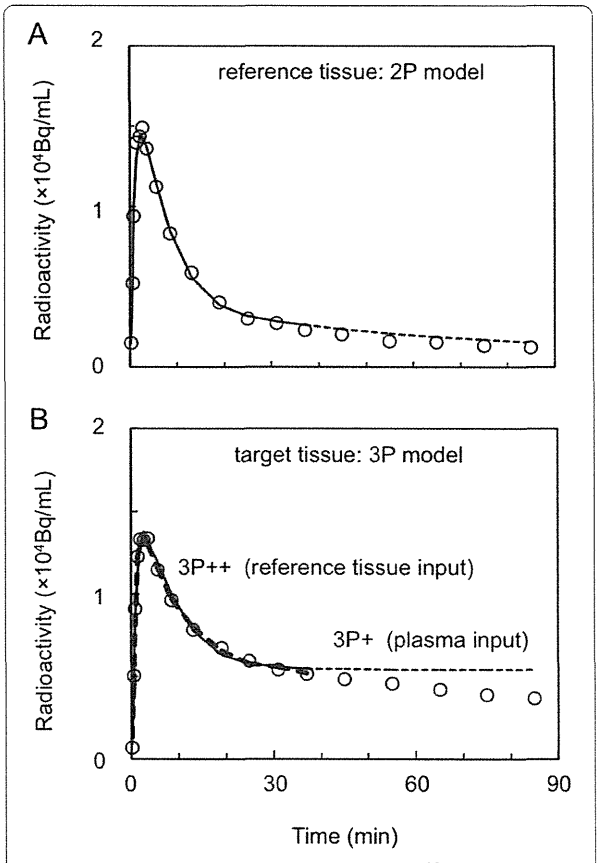

Figure 1 Reference and target tissue TACs in [^{11}C]PIB PET. (A) Cerebellar (reference tissue) data (open circle) up to 90 min in one AD subject and the fit of 40-min data to the 2P model (solid line). **(B)** Cerebral cortical (target tissue) data (open circle) in the same subject and the fits of 40-min data to the 3P model with arterial-plasma input (3P + analysis; solid line) or reference tissue input (3P++ analysis; dashed line). The dotted lines in **(A)** and **(B)** indicate the extension of the solid line from 40 to 90 min.

k_3 = 0.015/min) were estimated in 3P + analysis and R_1 = 0.897, k_2 = 0.158/min and k_3 = 0.011/min in 3P++ analysis.

Intra-subject k_3 correlation

Figure 2A is an example of the intra-subject k_3 correlation between 40-min 3P + (*X*-axis) and 3P++ (*Y*-axis) analyses, where the k_3 values of 15 ROIs, including the cerebellum (reference tissue in 3P++ analysis) from one particular NC subject or one particular AD subject, are shown. The regression lines and the coefficients of determination are $Y = 0.845X - 0.006$ ($r^2 = 0.972$) for the NC subject and $Y = 0.655X - 0.004$ ($r^2 = 0.982$) for the AD subject. Cerebellar k_3 values for both subjects are naturally calculated to be 0 in the 3P++ analysis. The slopes of the regression lines indicate the presence of negative bias in the 3P++ against the 3P + analysis.

Figure 2B shows the k_3 correlation between 90-min 4P (*X*-axis) and 40-min 3P++ (*Y*-axis) analyses in the same subjects. The regression lines are $Y = 0.590X - 0.005$ (r^2 = 0.953) for the NC subject and $Y = 0.338X + 0.000$ (r^2 = 0.907) for the AD subject. When the cerebellar data ($X = 0.008$, $Y = 0.000$) was removed from calculation for the AD subject, the regression line became $Y = 0.295X - 0.002$ with slightly larger r^2 (0.935; not shown in the figure). The slopes of the regression lines show that k_3 bias in 3P++ against 4P analysis is larger than that against 3P + analysis.

Inter-subject k_3 correlation

Figure 3A shows an example of the inter-subject k_3 correlation, where k_3 values for the left lateral temporal cortex from 30 subjects (15 NC + 15 AD) are compared between 40-min 3P + (*X*-axis) and 3P++ (*Y*-axis) analyses. The regression lines are $Y = 0.461X - 0.001$ (r^2 = 0.739) for all 30 subjects, $Y = 0.178X + 0.000$ ($r^2 = 0.151$) for the NC group alone, and $Y = 0.286X + 0.003$ (r^2 = 0.411) for the AD group alone; the latter two lines are not shown in the figure. The slopes of the regression lines also indicate the presence of negative biases in 3P++ against 3P + analysis.

Figure 3B shows the inter-subject correlation of left lateral temporal k_3 between 90-min 4P (*X*-axis) and 40-min 3P++ (*Y*-axis) analyses, where the regression line is $Y = 0.225X + 0.000$ ($r^2 = 0.711$) for all subjects. The lines of $Y = 0.090X + 0.001$ ($r^2 = 0.122$) for the NC group alone and $Y = 0.135X + 0.005$ ($r^2 = 0.513$) for the AD group alone were also calculated. The slopes of the regression lines show larger negative k_3 biases in 3P++ against 4P analysis than that shown in Figure 3A. The results in other cerebral regions were essentially the same as those in the left lateral temporal cortex.

Simulation on the effects of PET noise on k_3 CV

Figure 4 compares the noise sensitivity of k_3 estimates among the 90-min 4P, 40-min 3P+, and 3P++ analyses. In all three analyses, the k_3 CVs increased as the PET error became larger. The k_3 CV in 3P++ analysis was comparable to that in 3P + analysis and lower than that in 4P analysis; for example, k_3 CVs at 0.1 of noise level were 6.6% in 3P++, 7.0% in 3P+, and 11.4% in 4P analyses.

Simulation on the effects of target K_1 change on k_3 bias

Figure 5 shows the effects of K_1 change in the target ROI on the k_3 biases in the 90-min 4P, 40-min 3P+, and 3P++ analyses. The 4P analysis remained almost bias-free (+0.6%) within K_1 from 0.12 to 0.24 mL/g/min. 3P + and 3P++ analyses showed larger negative biases (−33% to −34% bias in 3P + and −33% to −35% bias in 3P++) compared with 4P analysis. Although 3P++ analysis showed slightly larger k_3 bias than 3P + analysis

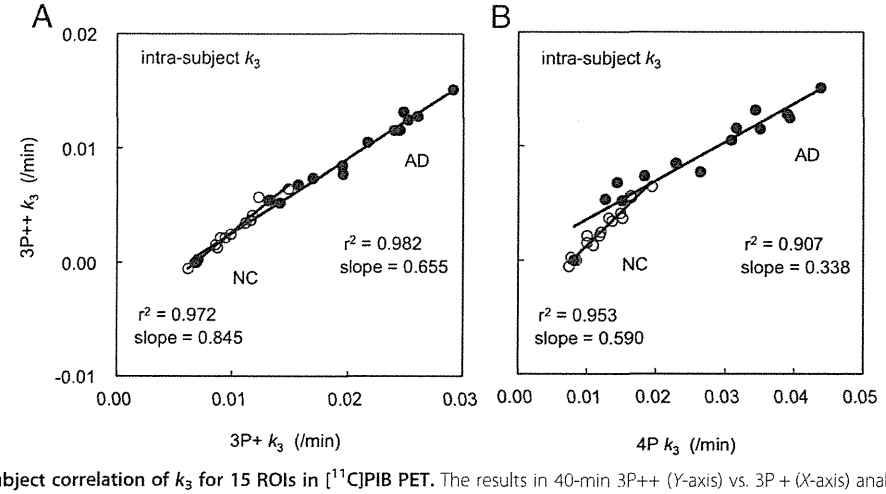

Figure 2 Intra-subject correlation of k_3 for 15 ROIs in [^{11}C]PIB PET. The results in 40-min 3P++ (*Y*-axis) vs. 3P + (*X*-axis) analyses **(A)** and 40-min 3P++ vs. 90-min 4P analyses **(B)** with one NC subject (open circle) and one AD subject (closed circle) are shown.

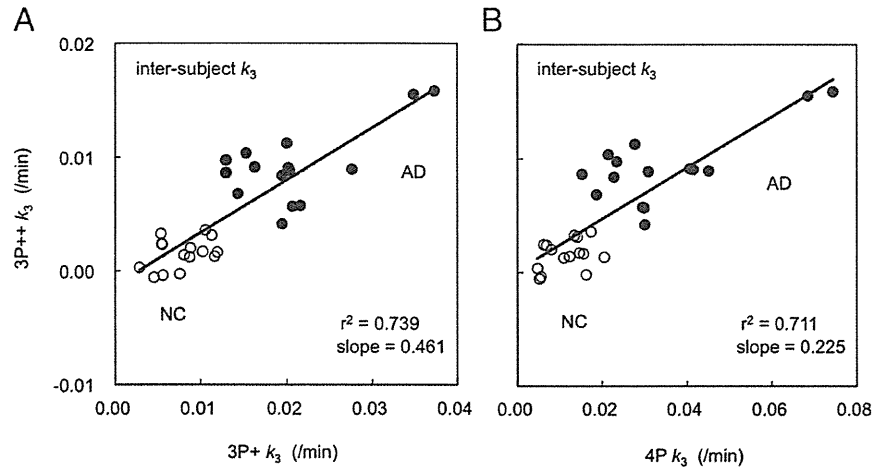

Figure 3 Inter-subject correlations of left lateral temporal k_3 in [^{11}C]PIB PET. The results in 40-min 3P++ (*Y*-axis) vs. 3P + (*X*-axis) analyses **(A)** and 40-min 3P++ vs. 90-min 4P analyses **(B)** with 30 subjects (15 NC, open circle; 15 AD, closed circle) are shown.

when K_1 was low (0.12 mL/g/min), k_3 bias in 3P++ analysis was almost the same as 3P + analysis.

Simulation on the effects of k_{2r} change on 3P++ analysis

In 3P++ analysis (Equation 1), k_{2r} was fixed at 0.178/min, though k_{2r} was not always the same among subjects (CV = 19%). Figure 6 shows the effects of individual k_{2r} change in 40-min 3P++ analysis. When k_{2r} was equal to the fixed value (0.18/min), 3P++ analysis was bias-free, relative to 3P + analysis. However, when k_{2r} was different from the fixed value, 3P++ analysis showed a negative k_3 bias relative to 3P + k_3. The k_{2r} effects were similar between NC ROI (k_3 = 0.018/min) and AD ROI (k_3 = 0.036/min); for example, the biases were −14.1% for NC and −12.1% for AD at k_{2r} = 0.12/min and −14.1% for NC and −11.3% for AD at k_{2r} = 0.24/min.

Simulation on the effects of k_{3r} change on 3P++ analysis

In 3P++ analysis we assume that k_{3r} = 0, that is, specific binding is negligible in the reference tissue. However, in all subjects examined, this assumption did not hold: the k_{3r} values in 40-min 3P + analysis were 0.008 ± 0.004/min in the AD group, 0.007 ± 0.002/min in the NC group, and 0.007 ± 0.003/min in the AD + NC group.

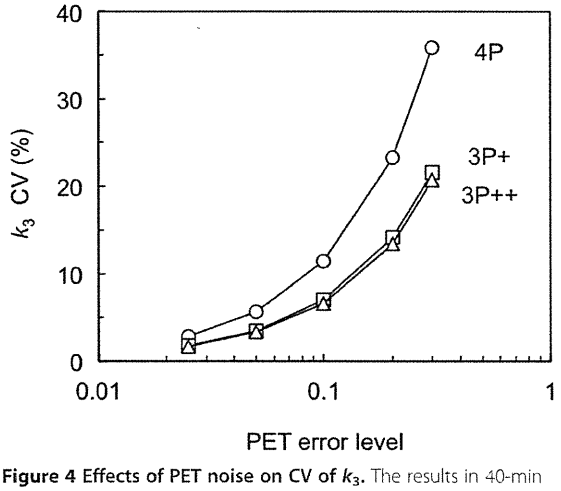

Figure 4 Effects of PET noise on CV of k_3. The results in 40-min 3P++ (open triangle), 40-min 3P + (open square), and 90-min 4P (open circle) analyses are shown. Five different PET noises (0.025 to 0.3) were added to the [^{11}C]PIB baseline TACs of the target ROI of the NC subjects. CV of k_3 was calculated from 100 k_3 estimates as CV (%) = (SD/mean) × 100.

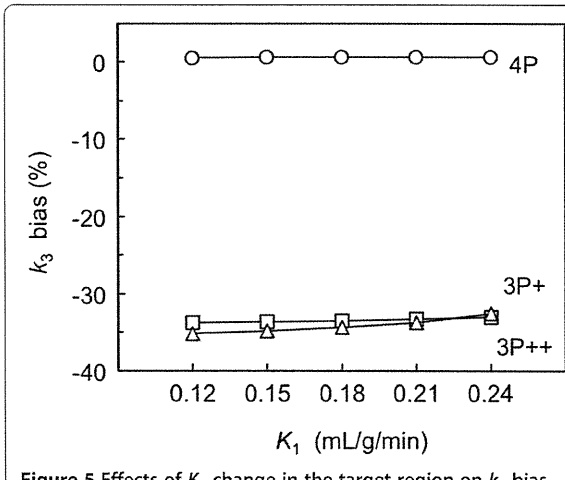

Figure 5 Effects of K_1 change in the target region on k_3 bias. The results in 40-min 3P++ (open triangle), 40-min 3P + (open square) and 90-min 4P (open circle) analyses are shown. Simulated target TACs were generated by 4P model with five different K_1 values (0.12 to 0.24 mL/g/min). The k_3 bias was calculated as bias (%) = (estimated k_3/true k_3 − 1) × 100.

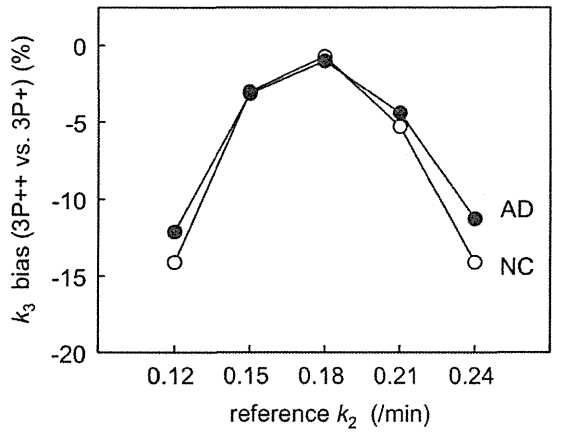

Figure 6 Effects of k_2 change in the reference region on k_3 bias in 40-min 3P++ analysis. Simulated target TACs were generated by 4P model with two different k_3 values (0.018/min for NC, open circle; 0.036/min for AD, closed circle). Simulated reference TACs were generated by 2P model with five different k_2 values (0.12 to 0.24/min). The k_3 bias in 3P++ analysis was expressed relative to 3P + analysis as bias (%) = (3P++ k_3/3P + k_3 − 1) × 100.

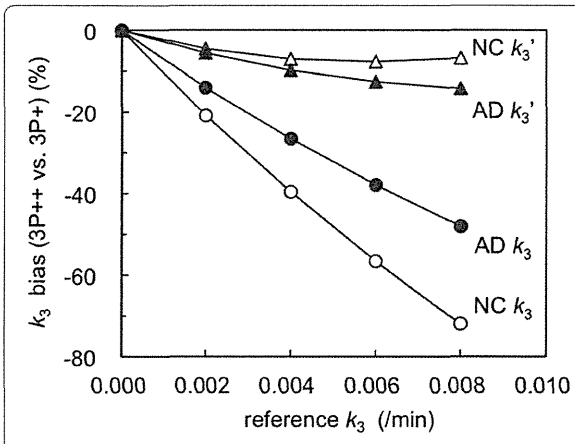

Figure 7 Effects of k_3 change in the reference region on k_3 bias in 40-min 3P++ analysis. Simulated target TACs were generated by 4P model with two different k_3 values (0.018/min for NC, open circle; 0.036/min for AD, closed circle). Simulated reference TACs were generated by 3P model with five different k_3 values (0 to 0.008/min). The k_3 bias in 3P++ analysis was expressed relative to 3P + analysis as bias (%) = (3P++ k_3/3P + k_3 − 1) × 100. Effects on bias in 3P++ k_3' relative to 3P + k_3 are also shown (NC, open triangle; AD, closed triangle), where 3P++ k_3' was calculated as (3P++ k_3') = (3P++ k_3) + reference k_3.

Figure 7 shows the effects of individual k_{3r} change (0 to 0.008/min) on 40-min 3P++ analysis. When k_{3r} was 0, 3P++ analysis was bias-free, relative to 3P + analysis. The k_3 biases (negative biases) increased as k_{3r} increased: −38% for NC and −27% for AD at k_{3r} = 0.004/min and −70% for NC and −48% for AD at k_{3r} = 0.008/min. The NC ROI (k_3 = 0.018/min) showed larger biases than the AD ROI (k_3 = 0.036/min). Figure 7 also shows the results of the simulation study on the relationship between 3P++ k_3' and 3P + k_3, where 3P++ k_3 was empirically corrected with individual k_{3r}. In this case, negative bias in 3P++ k_3' was significantly decreased compared to that in 3P++ k_3; for example, bias was decreased from −70% to −7% for NC, and from −48% to −15% for AD at k_{3r} = 0.008/min.

Figure 8 shows the correlation between 3P++ k_3' and 3P + k_3 using the same data as in Figure 3A, where 3P++ k_3 in Figure 3A was replaced by 3P++ k_3'. The regression line was $Y = 0.678X + 0.003$ ($r^2 = 0.975$) for all subjects, where X = 3P + k_3 and Y = 3P++ k_3'. The lines of $Y = 0.798X + 0.002$ ($r^2 = 0.897$) for the NC group alone and $Y = 0.620X + 0.004$ ($r^2 = 0.960$) for the AD group alone were also calculated. The determination coefficient was increased by this correction from 0.739 to 0.975. The slope of the regression line was also increased from 0.461 (Figure 3A) to 0.678 (Figure 8), which showed the reduction of negative bias in 3P++ analysis.

Discussion

Theoretical basis and merits of 3P++ analysis

The previous 3P + analysis allowed for estimating k_3 of moderately reversible ligands, where the 3P model was applied to early-phase (up to 30 to 40 min) PET data with arterial input function [13]. It was reported that when the 3P model was applied to 60-min PET scan data from [^{11}C]PIB (k_4 = 0.018/min) as a moderately reversible ligand, only a poor model fit was obtained [19]. Previous simulation studies on [^{11}C]PIB using information

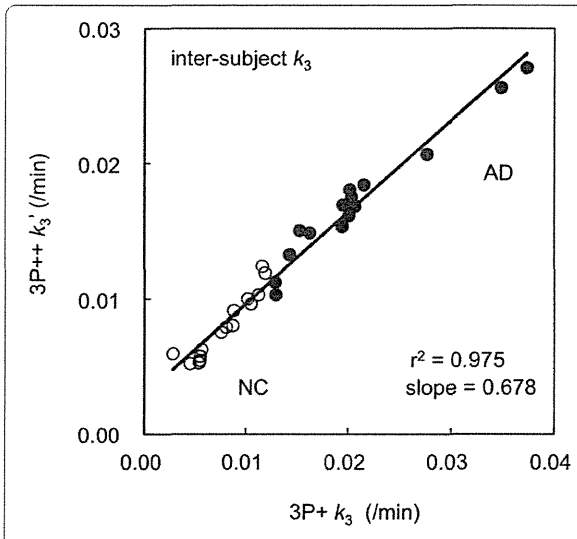

Figure 8 Inter-subject correlation of left lateral temporal k_3 in [^{11}C]PIB PET. The result in 40-min 3P++ (*Y*-axis) vs. 3P + (*X*-axis) analyses with 30 subjects (15 NC, open circle; 15 AD, closed circle) is shown. The k_3 estimates were empirically corrected as (3P++ k_3') = (3P++ k_3) + (individual cerebellar k_3 by 3P+).

density theory suggested that scan time reduction to 40 min would be necessary to obtain a good fit to the 3P model [13].

When 3P + or 3P++ analysis can be applied to a ligand, such ligand is specified as a moderately reversible ligand. This applicability is determined by the information function curves of k_3 and k_4 [13], and thus is dependent on the scan time as well as k_3 and k_4 values of the ligand in a ROI. Differentiation of a moderately reversible ligand from general reversible ligands is somewhat arbitrary, though we conveniently defined this with the k_4 value (≤0.03/min) in this study.

In the present study, the 3P + plasma input model was extended to the 3P++ reference tissue input model. The 3P++ analysis has three merits over previous methods. First, the PET scan time is short, usually less than 40 min, which may be important in PET studies with elderly or demented subjects. Secondly, the target parameter k_3 can be isolated from the other model parameters. Thirdly, neither arterial cannulation nor labor-intensive measurements of labeled metabolites are required.

One of the conventional models for the estimation of binding of [^{11}C]PIB is the Logan plot analysis [2], which employs data of long duration (more than 60 min). Noninvasive Logan analysis (distribution volume ratio) [6] requires late-phase (equilibrium-phase) PET data, whereas late-phase data are not necessary for 3P++ analysis. In the noninvasive Logan model or simplified reference tissue model [8], the K_1-to-k_2 ratio in the target and reference tissues is assumed to be equal. 3P++ analysis does not require such an assumption. Since 3P++ analysis is a kind of irreversible-model analysis, K_1 (R_1) and k_3 can be independently estimated (k_2 must be fixed to a certain constant).

Noise sensitivity of 3P++ analysis

Loss of PET data in short-scan 3P++ and 3P + analyses might be considered to deteriorate the precision of the k_3 estimate. In the present simulation for noise sensitivity, k_3 CV values in 40-min 3P++ and 3P + analyses were lower than (almost three fifths of) that in 90-min 4P analysis (Figure 4), which was in accordance with the previous report [13]. It is considered that the loss of PET data may be compensated for by the reduction in the number of free parameters from four in the 4P model to three in the 3P + and 3P++ models.

K_1 effect on 3P++ analysis

In the K_1 simulation, the stableness of k_3 estimation in changes of cerebral blood flow was investigated. The magnitudes of k_3 bias were independent of the K_1 change, ranging from 0.12 to 0.24 mL/g/min, in 3P++, 3P+, and 4P analyses (Figure 5). The 3P++ as well as 3P + and 4P analyses were less affected by K_1, which is owing to the capability of isolating the k_3 estimation. The 40-min 3P + analysis showed −33% k_3 bias relative to 90-min 4P analysis, which is in accordance with the previous report [13]. In this K_1 simulation, 3P++ k_3 showed negligible bias relative to 3P + k_3. These results suggested that in 3P++ analysis, the effects of ignoring vascular volume as well as numerical integration error due to discrete time points were not significant.

Causes of negative k_3 bias in 3P++ analysis

Firstly, the k_3 bias in 3P++ analysis originates from 3P model approximation. Our previous simulation study [13] showed that the 3P + analysis with 28-min scan had large negative k_3 bias relative to 4P analysis with 90-min scan; for example, there was about −22% to −24% bias to true k_3 (4P k_3) ranging from 0.01 to 0.04/min including NC and AD k_3. 3P++ analysis showed further negative k_3 bias relative to 3P + analysis due to the following two reasons.

Secondly, the bias is due to individual k_{2r} change from the fixed value in Equation 1. In 3P++ analysis, we also assumed that k_2 in the reference tissue was constant and was fixed at 0.178/min, which was the average k_2 value with the 3P + model. In simulation, negative k_3 bias was predicted when k_{2r} was larger or smaller than fixed k_2 (Figure 6). Each subject in the NC and AD groups had different k_2 values in the reference tissue, and it is considered that such biological variance as for reference tissue may result in a negative k_3 bias in 3P++ analysis, relative to 3P + analysis for [^{11}C]PIB.

Thirdly, the bias is due to the discrepancy between the model assumption and the actual reference ROI. The basic assumption (assumption 3) in 3P++ analysis is $k_{3r} = 0$. The working equation of 3P++ analysis (Equation 1) is derived under this assumption, and reference k_3 is naturally calculated to be 0. However, in 3P + analysis with [^{11}C]PIB, the cerebellum showed nonzero k_3 (0.007 ± 0.003/min in all 30 subjects). Thus, 3P++ k_3 is expected to be underestimated. Simulation studies showed that 3P++ analysis was bias-free for ideal reference with zero k_3 and that k_3 bias became larger as k_{3r} increased (Figure 7). When k_3 was replaced by k_3', negative bias was significantly decreased in the simulation (Figure 7), as well as the slope of the regression line between 3P++ and 3P + analyses being increased from 0.461 (Figure 3A) to 0.678 (Figure 8), which also suggested that nonzero k_{3r} caused underestimation of 3P++ k_3.

Correlation of k_3 between 3P++ and 3P + analyses

Strong intra-subject k_3 correlation was shown between 3P++ and 3P + analyses, and the rank-order of k_3 was almost the same between the two analyses (Figure 2A), suggesting the stability of both 3P++ and 3P + analyses.

The inter-subject k_3 correlation (r^2; Figure 3A) was significantly lower than the intra-subject correlation (Figure 2A). Such a lower inter-subject k_3 correlation

can be partly explained by the sample variance of cerebellar k_3. In order to explain this, k_3' was calculated for each subject. When k_3 was replaced by k_3', the determination coefficient between 3P++ and 3P + analyses was increased from 0.739 (Figure 3A) to 0.975 (Figure 8); the latter is comparable to r^2 of the intra-subject k_3 correlation (0.982; Figure 2A).

Such an estimation of parameter k_3' is not always practical, as 3P + analysis with arterial input function is necessary for individual cerebellar k_3 estimation. However, these results suggest that the lower r^2 in the inter-subject correlation compared with the intra-subject correlation is due to the sample variance of cerebellar k_3 and that 3P++ analysis itself is robust, as far as the reference is ideal.

Practically, the use of mean k_{3r} may be meaningful. When target k_3 is empirically corrected as corrected k_3 = estimated k_3 + mean cerebellar k_3, the absolute bias in target k_3 would decrease. However, the precision of target k_3 would not necessarily be improved owing to the variance of individual k_{3r}.

In addition to the nonzero effect of k_{3r}, inter-subject variation of k_{2r} from the fixed value (k_2 = 0.178/min) may also produce individually different k_3 bias in 3P++ analysis, resulting in lower inter-subject k_3 correlation between 3P + and 3P++ analyses.

Limitations of 3P++ analysis

When 3P++ analysis was applied to [^{11}C]PIB as an example of moderately reversible ligands, a somewhat lower inter-subject k_3 correlation (r^2 = 0.739 or 0.711; Figure 3A or Figure 3B) was shown between the 3P++ and 3P + or 4P analyses, respectively, across a k_3 range including NC and AD (3P + k_3, 0.004 to 0.040/min). The rank order of 3P++ k_3 also differed considerably from 3P + k_3 or 4P k_3. These results were mainly due to nonzero k_{3r} and the sample variance of both k_{2r} and k_{3r} as described above. The negative k_3 bias (3P++ vs. 3P+) was larger in NC ROI (−70%) than in AD ROI (−48%) when k_{3r} = 0.008/min (Figure 7). The previous report showed that the difference in k_3 bias (28-min 3P + vs. 90-min 4P) was small between NC ROI (−23%) and AD ROI (−24%) [13]. Therefore, the k_3 value in 3P++ analysis may be somewhat underestimated in the ROI with lower amyloid deposition compared to 3P + or 4P analysis.

In [^{11}C]PIB PET, 3P++ analysis may be inadequate for inter-subject k_3 comparison and useful only for intra-subject (inter-ROI) comparison or pre- vs. post-comparison in the same subject. 3P++ analysis would be more suitable for such reversible ligands that have moderate k_4 and reference tissue without specific binding.

Conclusions

The 3P++ analysis is a k_3 estimation method for moderately reversible PET ligands with a short scan time such as 40 min and without arterial blood sampling. Although the applicability of 3P++ method to [^{11}C]PIB PET may be restricted to intra-subject comparison, 3P++ analysis itself is robust. The 3P++ method would be useful for PET study with non-highly reversible ligands, as far as the reference tissue without specific binding is available.

Competing interests

The authors declare that they have no competing interests.

Authors' contributions

KS participated in clinical PET study and the simulation study, and drafted the manuscript. KF conceived of the study, participated in the simulation study, and helped to draft the manuscript. HS (Shinotoh), HS (Shimada), SH, and NT participated in clinical PET study and contributed to the discussion. TS, TI, and HI supervised the design and coordination of the study. All authors read and approved the final manuscript.

Acknowledgements

The authors thank the production team staff for the production of isotopes and the PET operation staff for the acquisition of PET images.

Author details

[1]Molecular Imaging Center, National Institute of Radiological Sciences, 4-9-1 Anagawa, Inage-ku, Chiba 260-8555, Japan. [2]Department of Psychiatry, Teikyo University Chiba Medical Center, 3426-3 Anesaki, Ichihara-shi, Chiba 299-0111, Japan. [3]Neurology Chiba Clinic, 1-2-12 Benten, Chuo-ku, Chiba 260-0045, Japan. [4]Section for Human Neurophysiology, Research Center for Frontier Medical Engineering, Chiba University, 1-33 Yayoi-cho, Inage-ku, Chiba 263-8522, Japan. [5]Department of Neurology, Graduate School of Medicine, Chiba University, 1-8-1 Inohana, Chuo-ku, Chiba 260-8677, Japan. [6]Bureau of Social Welfare and Public Health, Tokyo Metropolitan Government, 2-8-1 Nishi-shinjuku, Shinjuku-ku, Tokyo 163-8001, Japan.

Received: 4 October 2013 Accepted: 6 November 2013
Published: 16 November 2013

References

1. Mintun MA, Raichle ME, Kilbourn MR, Wooten GF, Welch MJ: **A quantitative model for the in vivo assessment of drug binding sites with positron emission tomography.** *Ann Neurol* 1984, **15**:217–227.
2. Logan J, Fowler JS, Volkow ND, Wolf AP, Dewey SL, Schlyer DJ, MacGregor RR, Hitzemann R, Bendriem B, Gatley SF, Christman DR: **Graphical analysis of reversible radioligand binding from time-activity measurements applied to [N-^{11}C-methyl]-(-)-cocaine PET studies in human subjects.** *J Cereb Blood Flow Metab* 1990, **10**:740–747.
3. Hume SP, Myers R, Bloomfield PM, Opacka-Juffry J, Cremer JE, Ahier RG, Luthra SK, Brooks DJ, Lammertsma AA: **Quantification of carbon-11-labeled racropride in rat striatum using positron emission tomography.** *Synapse* 1992, **12**:47–54.
4. Innis RB, Cunningham VJ, Delforge J, Fujita M, Gjedde A, Gunn RN, Holden J, Houle S, Huang SC, Ichise M, Iida H, Ito H, Kimura Y, Koeppe RA, Knudsen GM, Knuuti J, Lammertsma AA, Laruelle M, Logan J, Maguire RP, Mintun MA, Morris ED, Parsey R, Price JC, Slifstein M, Sossi V, Suhara T, Votaw JR, Wong DF, Carson RE: **Consensus nomenclature for in vivo imaging of reversibly binding radioligands.** *J Cereb Blood Flow Metab* 2007, **27**:1533–1539.
5. Ichise M, Ballinger JR, Golan H, Vines D, Luong A, Tsai S, Kung HF: **Noninvasive quantification of dopamine D2 receptors with iodine-123-IBF SPECT.** *J Nucl Med* 1996, **37**:513–520.
6. Lammertsma AA, Hume SP: **Simplified reference tissue model for PET receptor studies.** *Neuroimage* 1996, **4**:153–158.
7. Lammertsma AA, Bench CJ, Hume SP, Osman S, Gunn K, Brooks DJ, Frackowiak RSJ: **Comparison of methods for analysis of clinical [^{11}C] raclopride studies.** *J Cereb Blood Flow Metab* 1996, **16**:42–52.
8. Logan J, Fowler JS, Volkow ND, Wang GJ, Ding YS, Alexoff DL: **Distribution volume ratios without blood sampling from graphical analysis of PET data.** *J Cereb Blood Flow Metab* 1996, **16**:834–840.
9. Watabe H, Carson RE, Iida H: **The reference tissue model: three compartments for the reference region [abstract].** *Neuroimage* 2000, **11**:S12.

10. Wu Y, Carson RE: **Noise reduction in the simplified reference tissue model for neuroreceptor functional imaging.** *J Cereb Blood Flow Metab* 2002, **22**:1440–1452.
11. Koeppe RA, Frey KA, Snyder SE, Meyer P, Kilbourn MR, Kuhl DE: **Kinetic modeling of N-[^{11}C]methylpiperidin-4-yl propionate: alternatives for analysis of an irreversible positron emission tomography tracer for measurement of acetylcholinesterase activity in human brain.** *J Cereb Blood Flow Metab* 1999, **19**:1150–1163.
12. Namba H, Iyo M, Fukushi K, Shinotoh H, Nagatsuka S, Suhara T, Sudo Y, Suzuki K, Irie T: **Human cerebral acetylcholinesterase activity measured with positron emission tomography: procedure, normal values and effect of age.** *Eur J Nucl Med* 1999, **26**:135–143.
13. Sato K, Fukushi K, Shinotoh H, Shimada H, Tanaka N, Hirano S, Irie T: **A short-scan method for k_3 estimation with moderately reversible PET ligands: application of irreversible model to early-phase PET data.** *Neuroimage* 2012, **59**:3149–3158.
14. Price JC, Klunk WE, Lopresti BJ, Lu X, Hoge JA, Ziolko SK, Holt DP, Meltzer CC, DeKosky ST, Mathis CA: **Kinetic modeling of amyloid binding in humans using PET imaging and Pittsburgh Compound-B.** *J Cereb Blood Flow Metab* 2005, **25**:1528–1547.
15. Gunn RN, Gunn SR, Cunningham VJ: **Positron emission tomography compartmental models.** *J Cereb Blood Flow Metab* 2001, **21**:635–652.
16. McKhann G, Drachman D, Folstein M, Katzman R, Price D, Stadlan EM: **Clinical diagnosis of Alzheimer's disease: report of the NINCDS-ADRDA work group under the auspices of Department of Health and Human Services Task Force on Alzheimer's Disease.** *Neurology* 1984, **34**:939–944.
17. Mathis CA, Wang Y, Holt DP, Huang G-F, Debnath ML: **Synthesis and evaluation of ^{11}C-labeled 6-substituted 2-aryl benzothiazoles as amyloid imaging agents.** *J Med Chem* 2003, **46**:2740–2754.
18. Logan J, Fowler JS, Volkow ND, Ding YS, Wang GJ, Alexoff D: **A strategy for removing the bias in the graphical analysis method.** *J Cereb Blood Flow Metab* 2001, **21**:307–320.
19. Blomquist G, Englar H, Nordberg A, Ringheim A, Wall A, Forsberg A, Estrada M, Franberg P, Antoni G, Langstrom B: **Unidirectional influx and net accumulation of PIB.** *Open Neuroimag J* 2008, **2**:114–125.

doi:10.1186/2191-219X-3-76
Cite this article as: Sato *et al.*: Noninvasive k_3 estimation method for slow dissociation PET ligands: application to [^{11}C]Pittsburgh compound B. *EJNMMI Research* 2013 3:76.

Eur J Nucl Med Mol Imaging
DOI 10.1007/s00259-013-2620-7

ORIGINAL ARTICLE

Imaging of amyloid deposition in human brain using positron emission tomography and [^{18}F]FACT: comparison with [^{11}C] PIB

Hiroshi Ito · Hitoshi Shinotoh · Hitoshi Shimada · Michie Miyoshi · Kazuhiko Yanai · Nobuyuki Okamura · Harumasa Takano · Hidehiko Takahashi · Ryosuke Arakawa · Fumitoshi Kodaka · Maiko Ono · Yoko Eguchi · Makoto Higuchi · Toshimitsu Fukumura · Tetsuya Suhara

Received: 14 August 2013 / Accepted: 18 October 2013

Abstract
Purpose The characteristic neuropathological changes in Alzheimer's disease (AD) are deposition of amyloid senile plaques and neurofibrillary tangles. The ^{18}F-labeled amyloid tracer, [^{18}F]2-[(2-{(E)-2-[2-(dimethylamino)-1,3-thiazol-5-yl]vinyl}-1,3-benzoxazol-6-yl)oxy]-3-fluoropropan-1-ol (FACT), one of the benzoxazole derivatives, was recently developed. In the present study, deposition of amyloid senile plaques was measured by positron emission tomography (PET) with both [^{11}C]Pittsburgh compound B (PIB) and [^{18}F]FACT in the same subjects, and the regional uptakes of both radiotracers were directly compared.
Methods Two PET scans, one of each with [^{11}C]PIB and [^{18}F]FACT, were performed sequentially on six normal control subjects, two mild cognitive impairment (MCI) patients, and six AD patients. The standardized uptake value ratio of brain regions to the cerebellum was calculated with partial volume correction using magnetic resonance (MR) images to remove the effects of white matter accumulation.
Results No significant differences in the cerebral cortical uptake were observed between normal control subjects and AD patients in [^{18}F]FACT studies without partial volume correction, while significant differences were observed in [^{11}C]PIB. After partial volume correction, the cerebral cortical uptake was significantly larger in AD patients than in normal control subjects for [^{18}F]FACT studies as well as [^{11}C]PIB. Relatively lower uptakes of [^{11}C]PIB in distribution were observed in the medial side of the temporal cortex and in the occipital cortex as compared with [^{18}F]FACT. Relatively higher uptake of [^{11}C]PIB in distribution was observed in the frontal and parietal cortices.
Conclusion Since [^{18}F]FACT might bind more preferentially to dense-cored amyloid deposition, regional differences in cerebral cortical uptake between [^{11}C]PIB and [^{18}F]FACT might be due to differences in regional distribution between diffuse and dense-cored amyloid plaque shown in the autoradiographic and histochemical assays of postmortem AD brain sections.

Keywords Amyloid · Alzheimer · PET · FACT · PIB

H. Ito · H. Shinotoh · H. Shimada · M. Miyoshi · H. Takano · H. Takahashi · R. Arakawa · F. Kodaka · M. Ono · Y. Eguchi · M. Higuchi · T. Fukumura · T. Suhara
Molecular Imaging Center, National Institute of Radiological Sciences, Chiba, Japan

K. Yanai · N. Okamura
Department of Pharmacology, Tohoku University School of Medicine, Sendai, Japan

H. Ito (✉)
Biophysics Program, Molecular Imaging Center, National Institute of Radiological Sciences, 4-9-1 Anagawa, Inage-ku, Chiba 263-8555, Japan
e-mail: hito@nirs.go.jp

Published online: 14 November 2013

Introduction

Alzheimer's disease (AD) is the most common neurodegenerative dementia, and the characteristic neuropathological

changes in AD are deposition of amyloid senile plaques and neurofibrillary tangles (NFTs) [1]. The amyloid cascade hypothesis that deposition of amyloid protein would cause Alzheimer's pathology, e.g., the NFTs, cell loss, and vascular damage as a direct result of this deposition, has been proposed [2], and in vivo imaging of the deposition of amyloid senile plaques should contribute to the early diagnosis and evaluation for the treatment of AD. Several radiotracers to measure deposition of amyloid senile plaques by positron emission tomography (PET), e.g., [^{11}C]Pittsburgh compound B (PIB) [3, 4], [^{18}F]FDDNP [5], [^{11}C]SB-13 [6], [^{11}C]BF227 [7], [^{18}F]BAY94-9172 [8], [^{18}F]AV-45 [9], [^{11}C]AZD2184 [10], and [^{18}F]AZD4694 [11], were developed and used for investigation of the pathophysiology of AD.

[^{11}C]PIB, a benzothiazole derivative, is the most successful radiotracer for amyloid imaging and is widely used for clinical research of AD [12, 13]. However, cortical uptake of [^{11}C]PIB was often observed in healthy subjects with normal neuropsychological findings [14]. Since the fraction of soluble amyloid deposition in normal brain has been reported to be larger than that in AD brain [15], the cortical uptake of [^{11}C]PIB in normal subjects might be mainly due to binding to diffuse amyloid plaque.

Recently, [^{11}C]BF227, a benzoxazole derivative, was developed for in vivo imaging of amyloid senile plaques [7]. This radiotracer has been considered to bind more preferentially to dense-cored amyloid deposition than [^{11}C]PIB. It has been reported that synapse loss was accentuated within immature and mature plaques, but not within diffuse plaques [16], and the neuropathology of AD is characterized by cortical neuritic plaque containing dense-cored amyloid deposition [17]. Thus, a selective radiotracer for neuritic amyloid plaque might be useful for distinguishing the normal aging process from AD.

The ^{18}F-labeled amyloid tracer, [^{18}F]2-[(2-{(E)-2-[2-(dimethylamino)-1,3-thiazol-5-yl]vinyl}-1,3-benzoxazol-6-yl)oxy]-3-fluoropropan-1-ol (fluorinated amyloid imaging compound of Tohoku University, [^{18}F]FACT), one of the benzoxazole derivatives with a structure similar to [^{11}C]BF227, was recently developed [18, 19]. For [^{18}F]FACT, rapid accumulation and rapid washout were observed in the brains of both normal control subjects and AD patients, indicating its suitability as an amyloid imaging tracer in PET measurements [18]. Regional distribution similar to that of [^{11}C]BF227 was also observed. In the present study, deposition of amyloid senile plaques was measured by PET with both [^{11}C]PIB and [^{18}F]FACT in the same subjects including normal control subjects, mild cognitive impairment (MCI) patients, and AD patients. The binding and regional distribution of both radiotracers were directly compared to elucidate the binding characteristics of [^{18}F]FACT. To identify pathological aggregates providing major binding components for [^{11}C]PIB and [^{18}F]FACT, comparative autoradiographic and histochemical assays of postmortem AD brain sections were also performed.

Materials and methods

Subjects

Six normal control subjects (50–74 years old), two MCI patients (69 and 77 years old), and six AD patients (70–81 years old) were recruited (Table 1). All AD patients were diagnosed according to the National Institute of Neurological and Communicative Diseases and Stroke/Alzheimer's Disease and Related Disorders Association (NINCDS-ADRDA) criteria [20]. All subjects were classified according to the Clinical Dementia Rating (CDR) scale [21]. The normal control subjects corresponded to 0, the MCI patients to 0.5, and the AD subjects to 0.5, 1, or 2 on the CDR scale. The Mini-Mental State Examination (MMSE) was performed for all subjects [22]. No subjects had notable organic lesions in the brain according to magnetic resonance (MR) imaging. The normal control subjects were cognitively unimpaired and free from medications having central nervous action. The study was approved by the Ethics and Radiation Safety Committees of the National Institute of Radiological Sciences, Chiba, Japan. Written informed consent was obtained from all subjects or from their spouses or other close family members.

PET procedures

All PET studies were performed with SET-3000GCT/X (Shimadzu Corp., Kyoto, Japan) [23], which provides 99

Table 1 Profiles of subjects

Subject group	Subject no.	Age (years)	Sex	MMSE score
Normal control	NC1	70	F	29
	NC2	73	M	29
	NC3	74	M	29
	NC4	50	M	28
	NC5	61	M	28
	NC6	67	F	30
MCI	MCI1	77	F	26
	MCI2	69	M	24
AD	AD1	76	F	12
	AD2	71	M	19
	AD3	81	F	19
	AD4	70	F	15
	AD5	76	F	22
	AD6	80	F	24

sections with an axial field of view of 26 cm. Intrinsic spatial resolution was 3.4 mm in-plane and 5.0 mm full-width at half-maximum (FWHM) axially. With a Gaussian filter (cutoff frequency: 0.3 cycle/pixel), the reconstructed in-plane resolution was 7.5 mm FWHM. Data were acquired in three-dimensional mode. Scatter correction was done by a hybrid scatter correction method based on acquisition with a dual-energy window setting [24]. A 4-min transmission scan using a ^{137}Cs line source was performed for correction of attenuation.

Two PET scans, one each with [^{11}C]PIB and [^{18}F]FACT, were performed sequentially. After intravenous rapid bolus injection of [^{11}C]PIB, dynamic PET scanning was performed for 70 min. Then, 50 min after the end of the [^{11}C]PIB PET measurement, dynamic PET scanning was performed for 60 min after intravenous rapid bolus injection of [^{18}F]FACT. The frame sequence consisted of six 10-s frames, three 20-s frames, two 1-min frames, two 3-min frames, and twelve 5-min frames for [^{11}C]PIB and six 10-s frames, three 20-s frames, two 1-min frames, two 3-min frames, and ten 5-min frames for [^{18}F]FACT. Injected radioactivity was 332–493 MBq and 160–233 MBq for [^{11}C]PIB and [^{18}F]FACT, respectively. Specific radioactivity was 51–134 GBq/μmol and 59–494 GBq/μmol for [^{11}C]PIB and [^{18}F]FACT, respectively. [^{18}F]FACT was produced according to the literature [18].

MR imaging procedures

All MR imaging studies were performed with a 1.5-T MR scanner (Philips Medical Systems, Best, The Netherlands). Three-dimensional volumetric acquisition of a T1-weighted gradient echo sequence produced a gapless series of thin transverse sections (echo time 9.2 ms, repetition time 21 ms, flip angle 30°, field of view 256 mm, acquisition matrix 256 × 256, slice thickness 1 mm).

Calculation of parametric images

For both [^{11}C]PIB and [^{18}F]FACT studies, standardized uptake value (SUV) images were calculated from time-integrated radioactivity images by normalizing tissue radioactivity concentration with injected dose per body weight. The integration intervals were 50–70 min and 40–60 min for [^{11}C]PIB and [^{18}F]FACT, respectively. Since the cerebellum can be used as a reference brain region lacking fibrillar amyloid plaques [7, 25], the SUV ratio (SUVR) images, indicating amyloid deposition, were calculated as follows:

$$SUVR = SUV_{brain}/SUV_{cerebellum} \quad (1)$$

where SUV_{brain} and $SUV_{cerebellum}$ are SUV in brain regions and the cerebellum, respectively. Although the integration interval of 30–40 min including the peak equilibrium [26] was used for calculation of SUVR in the previous report with [^{18}F]FACT, they showed that almost the same SUVR could be obtained using the integration interval of 40–60 min corresponding to the late time phase after injection of [^{18}F]FACT [18]. Thus, the integration intervals corresponding to the late time phase were used for both [^{11}C]PIB and [^{18}F]FACT in the present study.

Data analysis

All MR images were coregistered to the PET images with the Statistical Parametric Mapping (SPM2) system [27]. MR images were transformed into standard brain size and shape by linear and nonlinear parameters by SPM2 (anatomic standardization). The brain templates used in SPM2 for anatomic standardization were T1 templates for MR images, i.e., Montreal Neurological Institute (MNI)/International Consortium for Brain Mapping (ICBM) 152 T1 templates as supplied with SPM2. All PET images were also transformed into standard brain size and shape by using the same parameters as the MR images. Thus, brain images of all subjects had the same anatomic format. Gray matter, white matter, and cerebrospinal fluid images were segmented and extracted from all anatomically standardized MR images by applying voxel-based morphometry methods with the SPM2 system [28]. These segmented MR images indicate the tissue fraction of gray or white matter per voxel (ml/ml). All anatomically standardized PET, gray matter, and white matter images were smoothed with an 8-mm FWHM isotropic Gaussian kernel, because final spatial resolution of the PET camera was approximately 8 mm FWHM.

Regions of interest (ROIs) were drawn on all anatomically standardized PET, gray matter, and white matter images with reference to the T1-weighted MR image. Elliptical ROIs (8 × 32 mm) were defined for the cerebellar cortex, parahippocampal gyrus including hippocampus, posterior region of the cingulate gyrus, base sides of frontal cortex, lateral side of temporal cortex, parietal cortex, cuneus of occipital cortex, and centrum semiovale.

Partial volume correction

SUV values are affected by the nonspecific accumulation of radiotracer in white matter because of the limited spatial resolution of the PET scanner. The SUV values per gray matter fraction in an ROI for cerebral cortical regions were calculated. The SUV value in an ROI can be expressed as follows [29, 30]:

$$SUV = SUV_{gray} \cdot TF_{gray} + SUV_{white} \cdot TF_{white} \quad (2)$$

where SUV_{gray} and SUV_{white} are SUV in gray and white matter, respectively, and TF_{gray} and TF_{white} are the tissue fraction of gray and white matter (ml/ml), respectively. According to this equation, if SUV_{white} is given, SUV_{gray} can be calculated for a given TF_{gray} and TF_{white}, which are determined by voxel-based morphometry with MR imaging. To correct effects of spill-in and spillover of radioactivity between gray and white matter, gray and white matter images smoothed with an 8-mm FWHM isotropic Gaussian kernel almost the same as the final spatial resolution of the PET camera were used for this partial volume correction. In the present study, the SUV_{gray} values were calculated by assuming SUV_{white} to be equal to the SUV value in the centrum semiovale. From the SUV_{gray} values in brain regions and the cerebellum, SUVR values in gray matter ($SUVR_{gray}$) were calculated by Eq. 1.

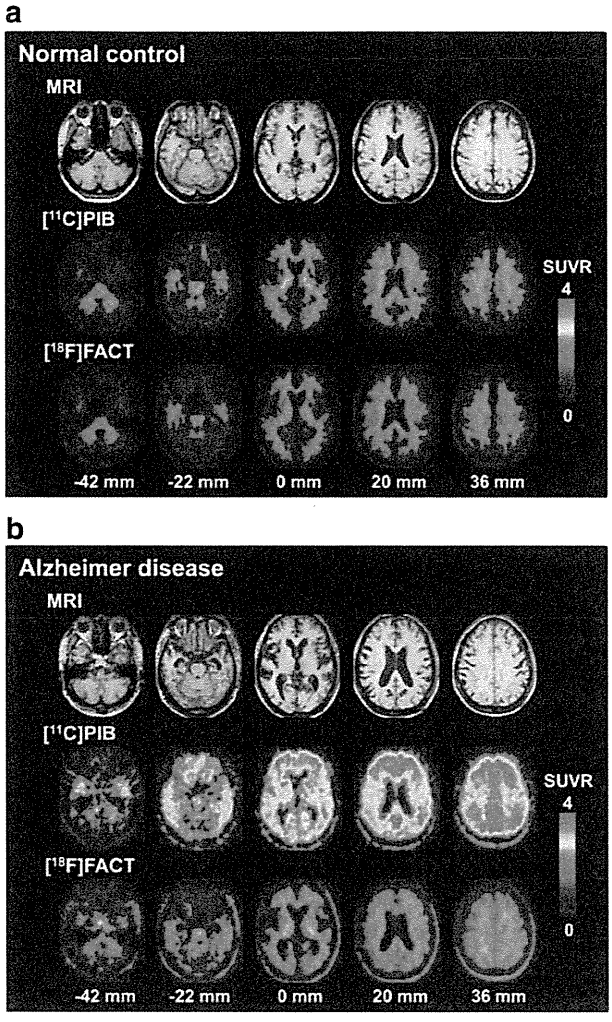

Fig. 1 Typical SUVR images of [^{11}C]PIB and [^{18}F]FACT studies and corresponding MR images (T1-weighted images) for a normal control subject (**a**) and an AD patient (**b**). Scale maximum and minimum values are 4 and 0 of SUVR. All images are transaxial sections parallel to the anterior-posterior commissure (AC-PC) line. Slice positions are −42, −22, 0, 20, and 36 mm from the AC-PC line. Anterior is at the top of the image and the subjects' right is on the left

Table 2 Average SUVR values of [^{11}C]PIB and [^{18}F]FACT studies

Region	[^{11}C]PIB	[^{18}F]FACT
Normal control subjects		
Frontal cortex	1.30±0.13	1.23±0.16
Temporal cortex	1.41±0.11	1.34±0.07
Parietal cortex	1.38±0.11	1.27±0.12
Occipital cortex	1.34±0.17	1.31±0.13
Parahippocampal gyrus	1.46±0.18	1.36±0.10
Posterior cingulate	1.64±0.15	1.49±0.08
Centrum semiovale	2.38±0.31	2.00±0.20
AD patients		
Frontal cortex	2.38±0.61**	1.14±0.13
Temporal cortex	2.14±0.37*	1.27±0.14
Parietal cortex	2.40±0.47*	1.29±0.11
Occipital cortex	1.84±0.27**	1.32±0.12
Parahippocampal gyrus	1.78±0.19***	1.31±0.07
Posterior cingulate	3.03±0.62*	1.61±0.18
Centrum semiovale	2.52±0.33	2.04±0.16

Values are shown as mean ± SD

Significant differences from normal control subjects (unpaired t test): *p <0.001; **p <0.01; ***p <0.05

Table 3 Average SUVR values in gray matter ($SUVR_{gray}$) of [^{11}C]PIB and [^{18}F]FACT studies

Region	[^{11}C]PIB	[^{18}F]FACT
Normal control subjects		
Frontal cortex	1.35±0.23	1.30±0.12
Temporal cortex	1.40±0.12	1.33±0.14
Parietal cortex	1.40±0.18	1.30±0.16
Occipital cortex	1.15±0.13	1.22±0.14
Parahippocampal gyrus	1.31±0.20	1.20±0.17
Posterior cingulate	1.60±0.25	1.44±0.18
AD patients		
Frontal cortex	4.91±1.63*	1.61±0.39****
Temporal cortex	3.53±0.98*	1.58±0.28****
Parietal cortex	4.57±1.47*	1.59±0.30****
Occipital cortex	3.10±1.28**	1.70±0.47***
Parahippocampal gyrus	2.72±0.58*	1.67±0.44***
Posterior cingulate	5.30±1.40*	2.02±0.43***

Values are shown as mean ± SD

Significant differences from normal control subjects (unpaired t test): *p <0.001; **p <0.01; ***p <0.05; ****p <0.1

Autoradiographic and histochemical assays of postmortem brain slices

Formalin-fixed, paraffin-embedded sections were generated from brains of patients with definite AD (generously provided by Dr. Trojanowski and Dr. Lee, University of Pennsylvania). Six-μm-thick slices were incubated in 50 mM Tris-HCl buffer (pH 7.4) containing 5 % ethanol and [^{11}C]PIB (250 MBq/l, approximately 5 nM) at room temperature for 60 min. Nonspecific binding was determined in the presence of 10 μM of nonradioactive PIB. Following the reaction, the samples were rinsed with ice-cold Tris-HCl buffer twice for 2 min and dipped into ice-cold water for 10 s. The slices were subsequently dried under warm blowing air and contacted to an imaging plate (Fujifilm, Tokyo, Japan) for 2 h. The imaging plate data were scanned with a BAS-5000 system (Fujifilm). The intensity of radioactive signals was measured by MultiGauge® software (Fujifilm). These sections were then

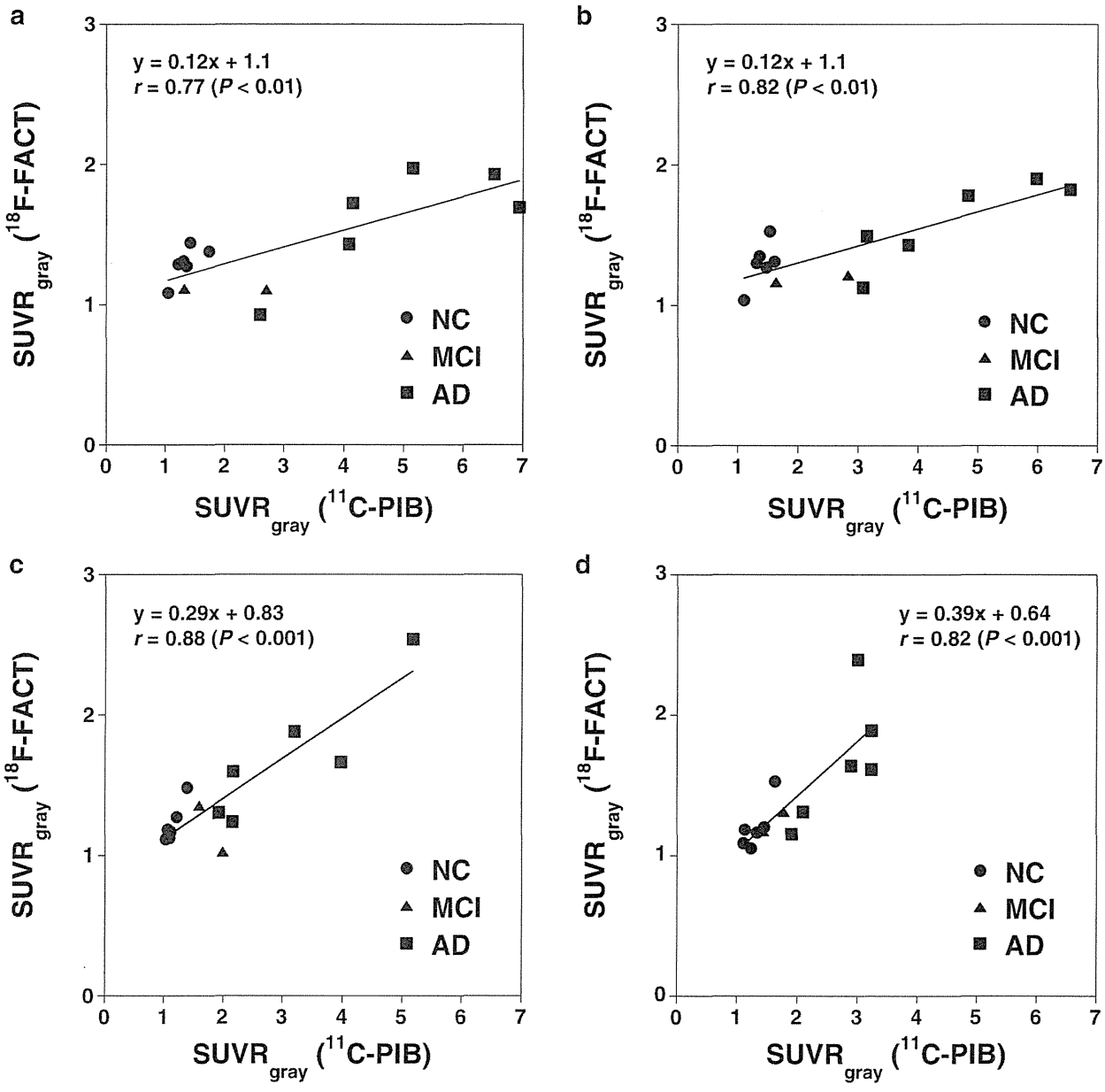

Fig. 2 The relationships of SUVR values in gray matter ($SUVR_{gray}$) between [^{11}C]PIB and [^{18}F]FACT studies for all subjects including normal control subjects (*NC*), mild cognitive impairment patients (*MCI*), and Alzheimer's disease patients (*AD*) in the frontal (**a**), parietal (**b**), occipital cortices (**c**), and parahippocampal gyrus (**d**)

labeled with [^{18}F]FACT 2 weeks after [^{11}C]PIB autoradiography. Briefly, the samples were reacted with [^{18}F]FACT (1 GBq/l, approximately 10 nM) dissolved in a reaction buffer identical to that used for [^{11}C]PIB at room temperature for 60 min. Nonspecific binding was determined in the presence of 10 μM of nonradioactive FACT. Tissue sections were then processed as in [^{11}C]PIB autoradiography and were contacted to an imaging plate for 15 min.

After radioactivity was allowed to decay, brain sections used for the autographic assay were fixed with 4 % paraformaldehyde in phosphate-buffered saline and were stained with 0.01 % (E,E)-1-fluoro-2,5-bis(3-hydroxycarbonyl-4-hydroxy)styrylbenzene (FSB, Dojindo Laboratories, Kumamoto, Japan), a fluorescent amyloid-binding compound, as described elsewhere [31]. Microscopic imaging was performed with an all-in-one microscope/digital camera (BZ-9000, Keyence, Osaka, Japan).

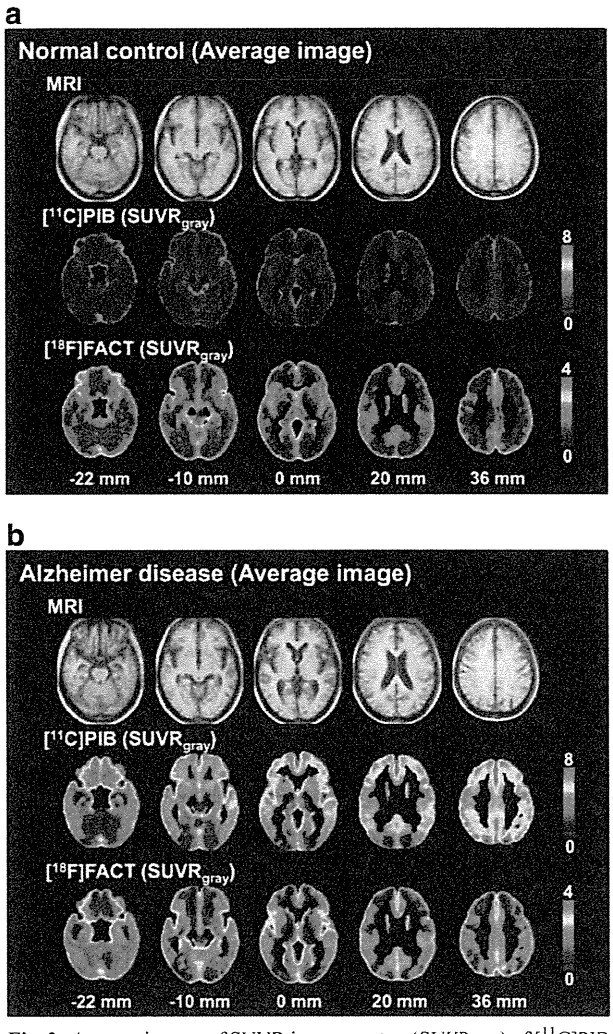

Fig. 3 Average images of SUVR in gray matter ($SUVR_{gray}$) of [^{11}C]PIB and [^{18}F]FACT studies and corresponding average MR images (T1-weighted images) for normal control subjects (**a**) and AD patients (**b**). Scale maximum and minimum values are 8 and 0 of $SUVR_{gray}$ for [^{11}C]PIB and 4 and 0 for [^{18}F]FACT studies. All images are transaxial sections parallel to the anterior-posterior commissure (AC-PC) line. Slice positions are −22, −10, 0, 20, and 36 mm from the AC-PC line. Anterior is at the top of the image and the subjects' right is on the left

Results

Typical SUVR images of [^{11}C]PIB and [^{18}F]FACT studies for a normal control subject are shown in Fig. 1a. Nonspecific accumulation in white matter was observed for both [^{11}C]PIB and [^{18}F]FACT. Typical SUVR images of [^{11}C]PIB and [^{18}F]FACT studies from an AD patient are shown in Fig. 1b. In AD patients, the cortical uptake indicating amyloid deposition was observed for both [^{11}C]PIB and [^{18}F]FACT. In the visual assessment of SUVR images, all normal control subjects and one of the MCI patients were diagnosed as negative for specific accumulation of [^{11}C]PIB, while all AD patients and the other MCI patient were diagnosed as positive.

The SUVR values of [^{11}C]PIB and [^{18}F]FACT studies in normal control subjects and AD patients are shown in Table 2. In [^{11}C]PIB studies, the SUVR values in all cerebral cortical regions were significantly larger in AD patients than in normal control subjects. However, in [^{18}F]FACT studies, no significant differences were observed between normal control subjects and AD patients in any of the brain regions.

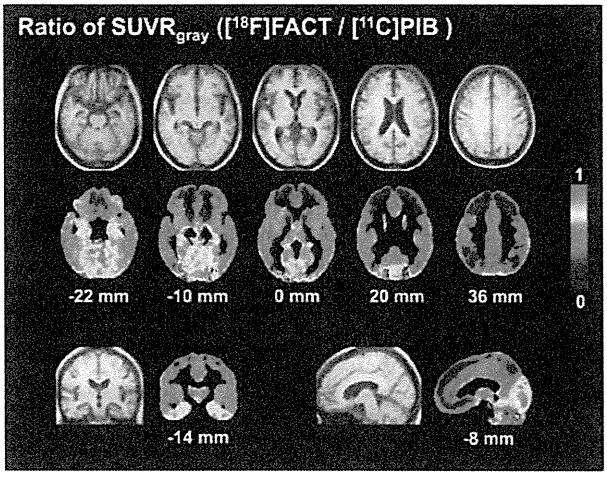

Fig. 4 Average images of ratio of SUVR in gray matter ($SUVR_{gray}$) of [^{18}F]FACT to [^{11}C]PIB studies for AD patients and corresponding average MR images (T1-weighted images). Scale maximum and minimum values are 1 and 0 of ratio. All transaxial images are parallel to the anterior-posterior commissure (AC-PC) line. Slice positions are −22, −10, 0, 20, and 36 mm from the AC-PC line. Anterior is at the top of the image and the subjects' right is on the left. The coronal image is perpendicular to the AC-PC line and its slice position is −14 mm (posterior side) from the AC. The subjects' right is on the left of the image. The sagittal image is parallel to the AC-PC line and its slice position is −8 mm (left side) from the AC-PC line. Anterior is on the left of the image

The $SUVR_{gray}$ values of [^{11}C]PIB and [^{18}F]FACT studies in normal control subjects and AD patients are shown in Table 3. In [^{11}C]PIB studies, the $SUVR_{gray}$ values in all cerebral cortical regions were significantly larger in AD patients than in normal control subjects. In [^{18}F]FACT studies, the $SUVR_{gray}$ value in the occipital cortex, parahippocampal gyrus, and posterior cingulate was significantly larger in AD patients than in normal control subjects. Trends of larger $SUVR_{gray}$ values in AD patients than in normal control subjects were observed in the frontal, temporal, and parietal cortices in the [^{18}F]FACT studies.

The relationships of $SUVR_{gray}$ values between [^{11}C]PIB and [^{18}F]FACT studies for all subjects are shown in Fig. 2. Significant positive correlations were observed in all brain regions. The slopes of linear regression lines (X: [^{11}C]PIB, Y: [^{18}F]FACT) ranged from 0.12 to 0.39. The greatest slopes were observed in the parahippocampal gyrus and occipital cortex, indicating relatively lower $SUVR_{gray}$ of [^{11}C]PIB and relatively higher $SUVR_{gray}$ of [^{18}F]FACT in these regions.

Average images of $SUVR_{gray}$ of [^{11}C]PIB and [^{18}F]FACT studies for normal control subjects and AD patients are shown in Fig. 3. Average images of the ratio of $SUVR_{gray}$ of [^{18}F]FACT to [^{11}C]PIB studies for AD patients are shown in Fig. 4. Relatively lower $SUVR_{gray}$ values of [^{11}C]PIB in distribution were observed in the medial side of the temporal cortex including the parahippocampal gyrus and occipital cortex as compared with [^{18}F]FACT. Relatively higher $SUVR_{gray}$ values of [^{11}C]PIB in distribution were observed in the frontal and parietal cortices.

The relationships between MMSE scores and $SUVR_{gray}$ of [^{11}C]PIB or [^{18}F]FACT studies for all AD patients and the one MCI patient positive for specific accumulation of [^{11}C]PIB are shown in Fig. 5. Significant positive correlations were observed in the temporal cortex for [^{11}C]PIB and in the frontal, parietal, and occipital cortices for [^{18}F]FACT. No significant correlation was observed in the parahippocampal gyrus and posterior cingulate for both [^{11}C]PIB and [^{18}F]FACT.

We then sought to identify pathological aggregates providing major binding components for [^{11}C]PIB and [^{18}F]FACT by comparative autoradiographic and histochemical assays of postmortem AD brain sections. Double autoradiographic labeling demonstrated distinct distribution of binding sites for these two radiotracers (Fig. 6a–c). Radio signals for [^{18}F]FACT were primarily observed in the hippocampal CA1 sector and subiculum besides white matter, in contrast to those for [^{11}C]PIB, which were most intense in the neocortex followed by the parahippocampal gyrus. No noticeable radiolabeling of [^{11}C]PIB and [^{18}F]FACT was detected in the hippocampal CA2 sector harboring numerous NFTs but few plaques (Fig. 6d), while [^{18}F]FACT signals in the CA1 and subiculum appeared to be associated with classic (dense-cored/neuritic) and compact plaques heavily deposited in these areas (Fig. 6e). Diffuse plaques, which were weakly labeled with FSB but involved no overt dystrophic changes of neurites, coexisted with NFTs in the parahippocampal gyrus (Fig. 6f) and therefore could be a source of moderate signals for [^{11}C]PIB. The fusiform gyrus was dominated by coreless

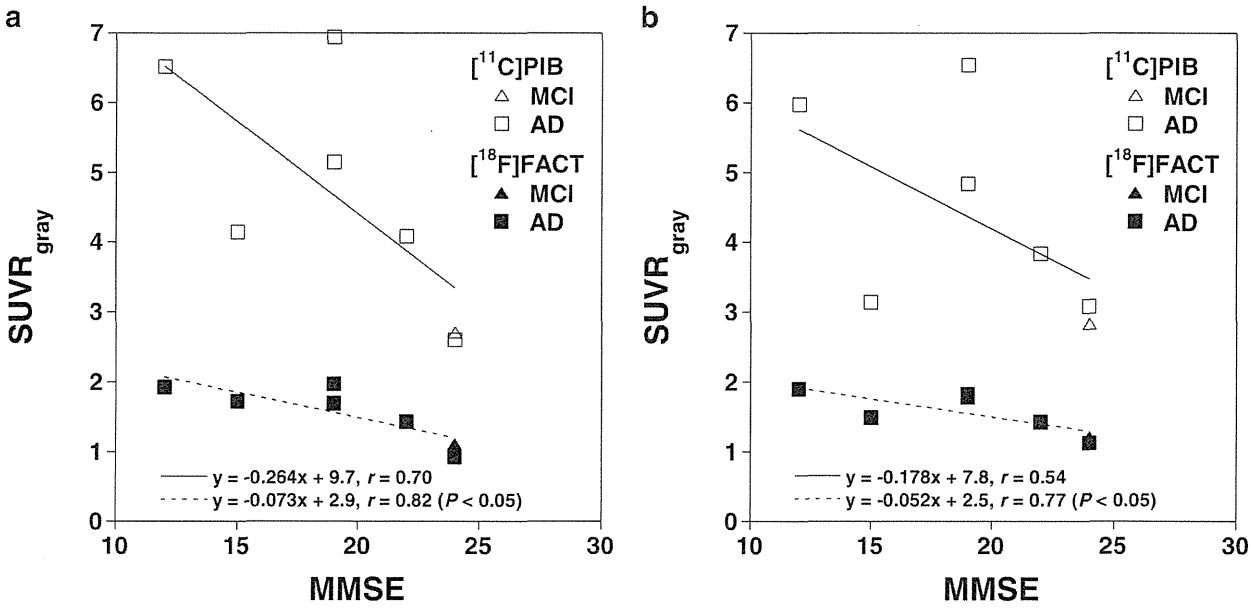

Fig. 5 The relationships between MMSE scores and SUVR values in gray matter ($SUVR_{gray}$) of [^{11}C]PIB or [^{18}F]FACT studies for all Alzheimer's disease patients (*AD*) and one patient with mild cognitive impairment (*MCI*) positive for specific accumulation of [^{11}C]PIB in the frontal (**a**) and parietal cortices (**b**)

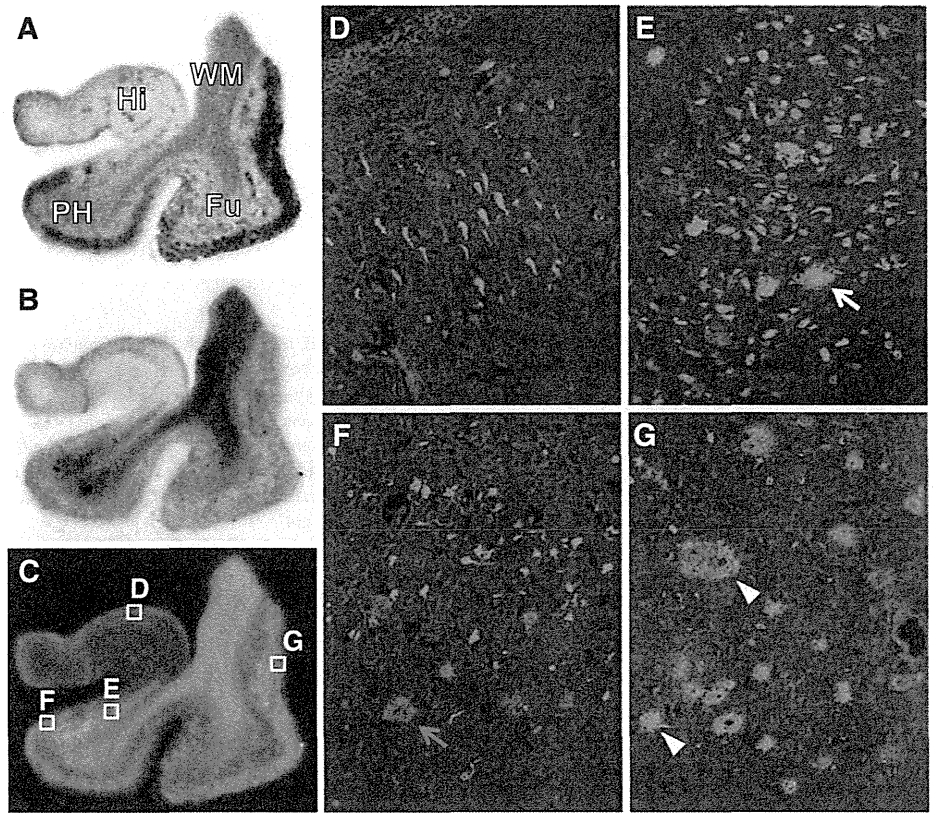

Fig. 6 Binding of [^{11}C]PIB and [^{18}F]FACT to distinct subtypes of senile plaques in AD patient brains. **a**, **b** Autoradiographic labeling of a single AD brain slice with [^{11}C]PIB (**a**) and [^{18}F]FACT (**b**). The section contains the hippocampus (*Hi*), parahippocampal gyrus (*PH*), fusiform gyrus (*Fu*), and white matter (*WM*). **c** Superimposition of autoradiograms displayed in **a** and **b**. *Red* and *green* signals indicate binding of [^{11}C]PIB and [^{18}F]FACT, respectively. *Squares* represent subregions from which photomicrographs shown in **d**–**g** were acquired. **d**–**g** Histofluorescence staining of amyloid lesions with FSB in the section used for autoradiography. NFTs with few plaques were observed in the hippocampal CA2 region (**d**), while classic and compact plaques (*white arrow*) with dense cores coexisted with NFTs in the subiculum (**e**). In the parahippocampal gyrus (**f**), NFTs were abundant in concurrence with diffuse plaques faintly illuminated with FSB (*red arrow*). The fusiform gyrus (**g**) was dominated by primitive plaques containing dystrophic neurites (*arrowheads*)

primitive plaques with FSB-positive neurites (Fig. 6g), accounting for the strong reactivity of [^{11}C]PIB with this region.

Discussion

While the SUVR values of [^{11}C]PIB were significantly larger in AD patients than in normal control subjects, no significant differences were observed between normal control subjects and AD patients in [^{18}F]FACT studies. In both [^{11}C]PIB and [^{18}F]FACT studies, nonspecific accumulation in white matter was observed, and this must hamper the quantitative analysis of cortical uptake of radiotracer due to the limited spatial resolution of the PET scanner. To remove the effects of white matter accumulation, $SUVR_{gray}$ values were calculated using gray and white matter images extracted from MR images according to the method developed by Müller-Gärtner et al. [29]. This partial volume correction technique was also originally used for estimation of cerebral blood flow per gray matter fraction in an ROI [30]. The $SUVR_{gray}$ values were larger in AD patients than in normal control subjects in both [^{11}C]PIB and [^{18}F]FACT studies. Since several radiotracers for amyloid imaging show the nonspecific accumulation in white matter [4, 7, 8, 18], such partial volume correction will be needed to estimate the deposition of amyloid senile plaques in cerebral cortices by PET. On the other hand, a recently developed radiotracer for amyloid deposits [^{11}C]AZD2184 which shows no conspicuous accumulation in white matter may not need such partial volume correction [10].

Although the $SUVR_{gray}$ values of [^{18}F]FACT were smaller than those of [^{11}C]PIB in AD patients, good correlations were observed in $SUVR_{gray}$ values between [^{11}C]PIB and [^{18}F]FACT studies, indicating the validity of [^{18}F]FACT as a radiotracer for amyloid imaging. Comparing $SUVR_{gray}$ images between [^{11}C]PIB and [^{18}F]FACT, relatively lower $SUVR_{gray}$ values of [^{11}C]PIB in distribution were observed in the parahippocampal gyrus and occipital cortex as compared with [^{18}F]FACT. Relatively higher $SUVR_{gray}$ values of

[^{11}C]PIB in distribution were also observed in the frontal and parietal cortices. A radiotracer for amyloid imaging, [^{11}C]BF227, has been considered to bind more preferentially to dense-cored amyloid deposition than [^{11}C]PIB [7]. [^{18}F]FACT has a structure similar to [^{11}C]BF227 and therefore it also binds more preferentially to dense-cored amyloid deposition [18]. If the cerebral cortical uptake of [^{11}C]PIB might be due to binding to both diffuse and dense-cored amyloid plaque [32], such regional differences in cerebral cortical uptake between [^{11}C]PIB and [^{18}F]FACT might be due to differences in regional distribution between diffuse and dense-cored amyloid plaque. In the present study, the autoradiographic and histochemical assays of postmortem AD brain sections also showed that [^{18}F]FACT signals were associated with classic (dense-cored/neuritic) and compact plaques, and diffuse plaques could be a source of moderate signals for [^{11}C]PIB. A histopathological study showed that diffuse amyloid plaques were not prominent in the occipital lobe as compared with the frontal and temporal lobes [33]. This might correspond to the relatively lower $SUVR_{gray}$ of [^{11}C]PIB in the occipital cortex as compared to that of [^{18}F]FACT observed in the present study.

It has been reported that synapse loss was accentuated within immature and mature plaques, but not within diffuse plaques [16]. Since [^{18}F]FACT might bind more preferentially to dense-cored amyloid plaques, [^{18}F]FACT binding might be an indicator of the severity of AD. In the present study, significant positive correlations were observed between MMSE scores and $SUVR_{gray}$ of [^{18}F]FACT in many of the neocortical regions, but not in [^{11}C]PIB as also shown in previous studies [34]. Although the number of the subjects is rather small to investigate the correlation between MMSE scores and $SUVR_{gray}$, this indicates that cortical accumulation of [^{18}F]FACT can reflect the severity of AD to a greater extent than [^{11}C]PIB.

In conclusion, deposition of amyloid senile plaques was measured by PET with both [^{11}C]PIB and [^{18}F]FACT in the same subjects, including normal control subjects, MCI patients, and AD patients. After partial volume correction to remove the effects of white matter accumulation, cerebral cortical uptake was larger in AD patients than in normal control subjects in both [^{11}C]PIB and [^{18}F]FACT studies. Regional differences in cerebral cortical uptake were observed between [^{11}C]PIB and [^{18}F]FACT, possibly due to differences in regional distribution between diffuse and dense-cored amyloid plaques.

Acknowledgments This study was supported in part by "Japan Advanced Molecular Imaging Program (J-AMP)" of the Ministry of Education, Culture, Sports, Science and Technology (MEXT), Japanese Government, a Grant-in-Aid for Comprehensive Research on Dementia (No. 11103404) from the Ministry of Health, Labour and Welfare, and a Grant-in-Aid from the Mitsubishi Pharma Research Foundation. We thank Mr. Katsuyuki Tanimoto and Mr. Takahiro Shiraishi for their assistance in performing the PET experiments at the National Institute of Radiological Sciences. We also thank Ms. Kazuko Suzuki and Ms. Izumi Izumida of the National Institute of Radiological Sciences for their help as clinical research coordinators.

Conflicts of interest None.

References

1. Braak H, Braak E. Neuropathological stageing of Alzheimer-related changes. Acta Neuropathol 1991;82:239–59.
2. Hardy JA, Higgins GA. Alzheimer's disease: the amyloid cascade hypothesis. Science 1992;256:184–5.
3. Mathis CA, Wang Y, Holt DP, Huang GF, Debnath ML, Klunk WE. Synthesis and evaluation of 11C-labeled 6-substituted 2-arylbenzothiazoles as amyloid imaging agents. J Med Chem 2003;46:2740–54.
4. Klunk WE, Engler H, Nordberg A, Wang Y, Blomqvist G, Holt DP, et al. Imaging brain amyloid in Alzheimer's disease with Pittsburgh Compound-B. Ann Neurol 2004;55:306–19.
5. Agdeppa ED, Kepe V, Liu J, Flores-Torres S, Satyamurthy N, Petric A, et al. Binding characteristics of radiofluorinated 6-dialkylamino-2-naphthylethylidene derivatives as positron emission tomography imaging probes for beta-amyloid plaques in Alzheimer's disease. J Neurosci 2001;21:RC189.
6. Ono M, Wilson A, Nobrega J, Westaway D, Verhoeff P, Zhuang ZP, et al. 11C-labeled stilbene derivatives as Abeta-aggregate-specific PET imaging agents for Alzheimer's disease. Nucl Med Biol 2003;30:565–71.
7. Kudo Y, Okamura N, Furumoto S, Tashiro M, Furukawa K, Maruyama M, et al. 2-(2-[2-Dimethylaminothiazol-5-yl]ethenyl)-6-(2-[fluoro]ethoxy)benzoxazole: a novel PET agent for in vivo detection of dense amyloid plaques in Alzheimer's disease patients. J Nucl Med 2007;48:553–61.
8. Rowe CC, Ackerman U, Browne W, Mulligan R, Pike KL, O'Keefe G, et al. Imaging of amyloid beta in Alzheimer's disease with 18F-BAY94-9172, a novel PET tracer: proof of mechanism. Lancet Neurol 2008;7:129–35.
9. Choi SR, Golding G, Zhuang Z, Zhang W, Lim N, Hefti F, et al. Preclinical properties of 18F-AV-45: a PET agent for Aβ plaques in the brain. J Nucl Med 2009;50:1887–94.
10. Nyberg S, Jönhagen ME, Cselényi Z, Halldin C, Julin P, Olsson H, et al. Detection of amyloid in Alzheimer's disease with positron emission tomography using [11C]AZD2184. Eur J Nucl Med Mol Imaging 2009;36:1859–63.
11. Cselényi Z, Jönhagen ME, Forsberg A, Halldin C, Julin P, Schou M, et al. Clinical validation of 18F-AZD4694, an amyloid-beta-specific PET radioligand. J Nucl Med 2012;53:415–24.
12. Buckner RL, Snyder AZ, Shannon BJ, LaRossa G, Sachs R, Fotenos AF, et al. Molecular, structural, and functional characterization of Alzheimer's disease: evidence for a relationship between default activity, amyloid, and memory. J Neurosci 2005;25:7709–17.
13. Engler H, Forsberg A, Almkvist O, Blomquist G, Larsson E, Savitcheva I, et al. Two-year follow-up of amyloid deposition in patients with Alzheimer's disease. Brain 2006;129:2856–66.
14. Rowe CC, Ng S, Ackermann U, Gong SJ, Pike K, Savage G, et al. Imaging β-amyloid burden in aging and dementia. Neurology 2007;68:1718–25.
15. Wang J, Dickson DW, Trojanowski JQ, Lee VM. The levels of soluble versus insoluble brain Aβ distinguish Alzheimer's disease from normal and pathologic aging. Exp Neurol 1999;158:328–37.

16. Masliah E, Terry RD, Mallory M, Alford M, Hansen LA. Diffuse plaques do not accentuate synapse loss in Alzheimer's disease. Am J Pathol 1990;137:1293–7.
17. Price JL. Diagnostic criteria for Alzheimer's disease. Neurobiol Aging 1997;18:S67–70.
18. Furumoto S, Okamura N, Furukawa K, Tashiro M, Ishikawa Y, Sugi K, et al. A 18F-labeled BF-227 derivative as a potential radioligand for imaging dense amyloid plaques by positron emission tomography. Mol Imaging Biol 2013;15:497–506.
19. Shidahara M, Tashiro M, Okamura N, Furumoto S, Furukawa K, Watanuki S, et al. Evaluation of the biodistribution and radiation dosimetry of the 18F-labelled amyloid imaging probe [18F]FACT in humans. EJNMMI Res 2013;3:32.
20. McKhann G, Drachman D, Folstein M, Katzman R, Price D, Stadlan EM. Clinical diagnosis of Alzheimer's disease: report of the NINCDS-ADRDA Work Group under the auspices of Department of Health and Human Services Task Force on Alzheimer's Disease. Neurology 1984;34:939–44.
21. Morris JC. The Clinical Dementia Rating (CDR): current version and scoring rules. Neurology 1993;43:2412–4.
22. Folstein MF, Folstein SE, McHugh PR. "Mini-mental state". A practical method for grading the cognitive state of patients for the clinician. J Psychiatr Res 1975;12:189–98.
23. Matsumoto K, Kitamura K, Mizuta T, Tanaka K, Yamamoto S, Sakamoto S, et al. Performance characteristics of a new 3-dimensional continuous-emission and spiral-transmission high-sensitivity and high-resolution PET camera evaluated with the NEMA NU 2-2001 standard. J Nucl Med 2006;47:83–90.
24. Ishikawa A, Kitamura K, Mizuta T, Tanaka K, Amano M, Inoue Y, et al. Implementation of on-the-fly scatter correction using dual energy window method in continuous 3D whole body PET scanning. IEEE Nucl Sci Symp Conf Rec 2005;5:2497–500.
25. Price JC, Klunk WE, Lopresti BJ, Lu X, Hoge JA, Ziolko SK, et al. Kinetic modeling of amyloid binding in humans using PET imaging and Pittsburgh Compound-B. J Cereb Blood Flow Metab 2005;25:1528–47.
26. Ito H, Hietala J, Blomqvist G, Halldin C, Farde L. Comparison of the transient equilibrium and continuous infusion method for quantitative PET analysis of [11C]raclopride binding. J Cereb Blood Flow Metab 1998;18:941–50.
27. Friston KJ, Frith CD, Liddle PF, Dolan RJ, Lammertsma AA, Frackowiak RS. The relationship between global and local changes in PET scans. J Cereb Blood Flow Metab 1990;10:458–66.
28. Ashburner J, Friston KJ. Voxel-based morphometry–the methods. Neuroimage 2000;11:805–21.
29. Müller-Gärtner HW, Links JM, Prince JL, Bryan RN, McVeigh E, Leal JP, et al. Measurement of radiotracer concentration in brain gray matter using positron emission tomography: MRI-based correction for partial volume effects. J Cereb Blood Flow Metab 1992;12:571–83.
30. Ito H, Inoue K, Goto R, Kinomura S, Taki Y, Okada K, et al. Database of normal human cerebral blood flow measured by SPECT: I. Comparison between I-123-IMP, Tc-99m-HMPAO, and Tc-99m-ECD as referred with O-15 labeled water PET and voxel-based morphometry. Ann Nucl Med 2006;20:131–8.
31. Higuchi M, Iwata N, Matsuba Y, Sato K, Sasamoto K, Saido TC. 19F and 1H MRI detection of amyloid beta plaques in vivo. Nat Neurosci 2005;8:527–33.
32. Ikonomovic MD, Klunk WE, Abrahamson EE, Mathis CA, Price JC, Tsopelas ND, et al. Post-mortem correlates of in vivo PiB-PET amyloid imaging in a typical case of Alzheimer's disease. Brain 2008;131:1630–45.
33. Yamaguchi H, Hirai S, Morimatsu M, Shoji M, Harigaya Y. Diffuse type of senile plaques in the brains of Alzheimer-type dementia. Acta Neuropathol 1988;77:113–9.
34. Jack Jr CR, Lowe VJ, Senjem ML, Weigand SD, Kemp BJ, Shiung MM, et al. 11C PiB and structural MRI provide complementary information in imaging of Alzheimer's disease and amnestic mild cognitive impairment. Brain 2008;131:665–80.

Please cite this article in press as: Maruyama et al., Imaging of Tau Pathology in a Tauopathy Mouse Model and in Alzheimer Patients Compared to Normal Controls, Neuron (2013), http://dx.doi.org/10.1016/j.neuron.2013.07.037

Imaging of Tau Pathology in a Tauopathy Mouse Model and in Alzheimer Patients Compared to Normal Controls

Masahiro Maruyama,[1,10] Hitoshi Shimada,[1,10] Tetsuya Suhara,[1] Hitoshi Shinotoh,[1] Bin Ji,[1] Jun Maeda,[1] Ming-Rong Zhang,[1] John Q. Trojanowski,[2] Virginia M.-Y. Lee,[2] Maiko Ono,[1] Kazuto Masamoto,[1] Harumasa Takano,[1] Naruhiko Sahara,[3,5,6] Nobuhisa Iwata,[4] Nobuyuki Okamura,[7] Shozo Furumoto,[7] Yukitsuka Kudo,[8] Qing Chang,[9] Takaomi C. Saido,[4] Akihiko Takashima,[3] Jada Lewis,[5,6] Ming-Kuei Jang,[9] Ichio Aoki,[1] Hiroshi Ito,[1] and Makoto Higuchi[1,*]

[1]Molecular Imaging Center, National Institute of Radiological Sciences, 4-9-1 Anagawa, Inage-ku, Chiba, Chiba 263-8555, Japan
[2]Center for Neurodegenerative Disease Research, University of Pennsylvania Perelman School of Medicine, Third Floor HUP-Maloney, 36th and Spruce Streets, Philadelphia, PA 19104, USA
[3]Laboratory for Alzheimer's Disease
[4]Laboratory for Proteolytic Neuroscience
RIKEN Brain Science Institute, 2-1 Hirosawa, Wako, Saitama 351-0198, Japan
[5]Center for Translational Research in Neurodegenerative Disease
[6]Department of Neuroscience
University of Florida, 1275 Center Drive, Gainesville, FL 32610, USA
[7]Department of Pharmacology, Tohoku University Graduate School of Medicine, 2-1 Seiryo-machi, Aoba-ku, Sendai, Miyagi 980-8575, Japan
[8]Clinical Research, Innovation and Education Center, Tohoku University Hospital, 1-1 Seiryo-machi, Aoba-ku, Sendai, Miyagi 980-8574, Japan
[9]Institute for Applied Cancer Science, MD Anderson Cancer Center, 1901 East Road, Houston, TX 77054, USA
[10]These authors contributed equally to this work
*Correspondence: mhiguchi@nirs.go.jp
http://dx.doi.org/10.1016/j.neuron.2013.07.037

SUMMARY

Accumulation of intracellular tau fibrils has been the focus of research on the mechanisms of neurodegeneration in Alzheimer's disease (AD) and related tauopathies. Here, we have developed a class of tau ligands, phenyl/pyridinyl-butadienyl-benzothiazoles/benzothiazoliums (PBBs), for visualizing diverse tau inclusions in brains of living patients with AD or non-AD tauopathies and animal models of these disorders. In vivo optical and positron emission tomographic (PET) imaging of a transgenic mouse model demonstrated sensitive detection of tau inclusions by PBBs. A pyridinated PBB, [^{11}C]PBB3, was next applied in a clinical PET study, and its robust signal in the AD hippocampus wherein tau pathology is enriched contrasted strikingly with that of a senile plaque radioligand, [^{11}C]Pittsburgh Compound-B ([^{11}C]PIB). [^{11}C]PBB3-PET data were also consistent with the spreading of tau pathology with AD progression. Furthermore, increased [^{11}C]PBB3 signals were found in a corticobasal syndrome patient negative for [^{11}C]PIB-PET.

INTRODUCTION

Hallmark pathologies of Alzheimer's disease (AD) are extracellular senile plaques consisting of aggregated amyloid β peptide (Aβ) and intraneuronal neurofibrillary tangles (NFTs) composed of pathological tau fibrils, while similar tau lesions in neurons and glia are also characteristic of other neurodegenerative disorders, such as progressive supranuclear palsy (PSP) and corticobasal degeneration (CBD), that are collectively referred to as tauopathies (Ballatore et al., 2007). The discovery of *tau* gene mutations in a familial form of tauopathy, known as frontotemporal dementia and parkinsonism linked to chromosome 17 (FTDP-17), and subsequent studies of transgenic (Tg) mice expressing human tau with or without these mutations, clearly implicate pathological tau in mechanisms of neurodegeneration in AD and related tauopathies (Ballatore et al., 2007). Thus, there is an urgent need for tau imaging techniques to complement Aβ amyloid imaging methods that now are widely used.

In vivo imaging modalities, as exemplified by positron emission tomography (PET) (Klunk et al., 2004; Small et al., 2006; Kudo et al., 2007; Maeda et al., 2007), optical scanning (Bacskai et al., 2003; Hintersteiner et al., 2005), and magnetic resonance imaging (MRI) (Higuchi et al., 2005), have enabled visualization of Aβ deposits in humans with AD and/or AD mouse models, and there has been a growing expectation that low-molecular-weight ligands for β-pleated sheet structures will also serve as molecular probes for tau amyloids. Although the majority of plaque-imaging agents used for clinical PET studies do not bind to tau lesions (Klunk et al., 2003), at least one radiolabeled β sheet ligand, [^{18}F]FDDNP, enables PET imaging of AD NFTs (Small et al., 2006). However, a relatively low contrast of in vitro autoradiographic and in vivo PET signals for [^{18}F]FDDNP putatively reflecting tau lesions does not allow a simple visual inspection of images for the assessment of tau pathologies in living subjects

Please cite this article in press as: Maruyama et al., Imaging of Tau Pathology in a Tauopathy Mouse Model and in Alzheimer Patients Compared to Normal Controls, Neuron (2013), http://dx.doi.org/10.1016/j.neuron.2013.07.037

(Small et al., 2006; Thompson et al., 2009). Thus, better tau radioligands with higher affinity for tau fibrils and/or less nonspecific binding to tissues are urgently needed to complement high-contrast senile plaque imaging agents, including widely studied [^{11}C]Pittsburgh Compound-B ([^{11}C]PIB) (Klunk et al., 2004) and United States Food and Drug Administration-approved [^{18}F]florbetapir (Yang et al., 2012). In addition, [^{18}F]FDDNP and several other candidate tau probes do not bind to tau inclusions in non-AD tauopathy brains without plaque deposition (Okamura et al., 2005) and therefore can be clinically characterized only in AD patients with comingled Aβ and tau amyloids. Hence, compounds that detect diverse tau aggregates, including tau inclusions in non-AD neurodegenerative diseases and tau Tg models, could be used to interrogate in vivo interactions between exogenous ligands and tau pathologies.

Here, we found that the lipophilicity of β sheet ligands is associated with their selectivity for tau versus Aβ fibrils and that the core dimensions of these chemicals are major determinants of their reactivity with a broad spectrum of tau aggregates in diverse tauopathies and mouse models of tau pathology. Building on these observations, we developed a series of fluorescent compounds capable of detecting diverse tau lesions using optical and PET imaging in living Tg mouse models of tauopathies. Finally, we identified a radiotracer that produced the highest contrast for tau inclusions in animal PET and used it in exploratory in vivo imaging studies of AD patients, providing clear demonstration of signal intensification in tau-rich regions, in sharp distinction to [^{11}C]PIB-PET data reflecting plaque deposition.

RESULTS

Identification of PBBs as Ligands for Diverse Tau Inclusions in Human Tauopathies

We screened an array of fluorescent chemicals capable of binding to β sheet conformations (see the Compounds subsection in the Experimental Procedures). Fluorescence labeling with these compounds were examined in sections of AD brains bearing Aβ and tau amyloids (Figures 1A and 2A) and non-AD tauopathy brains characterized by tau inclusions and few or no Aβ plaques (Figure 2). Amyloid PET tracers currently used for human PET studies, PIB (Klunk et al., 2004), and BF-227 (Kudo et al., 2007), tightly bound to senile plaques, while they only weakly reacted with AD NFTs (Figures 1A; Figure S1 available online). PET probes reported to selectively label tau aggregates, BF-158 (Okamura et al., 2005) and THK523 (Fodero-Tavoletti et al., 2011), detected AD NFTs (Figures 2A and S1) but microscopically detectable fluorescence signals produced by FDDNP, which are presumed to bind to both Aβ and tau fibrils (Small et al., 2006), were consistent with dense cores of classic plaques and distinct from tau lesions (Figures 2A and S1). None of the above-mentioned PET ligands were reactive with tau inclusions in non-AD tauopathies, such as Pick bodies in Pick's disease (Figures 2A and S1) and neuronal and glial fibrillary lesions in PSP and CBD (data not shown). By contrast, these pathologies were intensely labeled with a widely used amyloid dye, thioflavin-S, and a derivative of another classic amyloid dye Congo red, (E,E)-1-fluoro-2,5-bis(3-hydroxycarbonyl-4-hydroxy)styrylbenzene (FSB) (Higuchi et al., 2005; Maeda et al., 2007) (Figures 1, 2A, and S1), although these chemicals may not undergo efficient transfer through the blood-brain barrier (BBB) (Zhuang et al., 2001). Because compounds possessing a π-electron-conjugated backbone longer than 13Å exhibited affinities for pathological inclusions in a broad range of tauopathies, we examined binding of additional chemicals with a variety of structural dimensions to tau aggregates and found that affinity for non-AD tau inclusions could be attributed to a core structure with a specific extent ranging from 13 to 19 Å (Figure S1). Based on this view and the known fact that chemicals with a flat and slender backbone could pass through and attach to channel-like accesses in β-pleated sheets (Krebs et al., 2005), we developed a class of compounds, phenyl/pyridinyl-butadienyl-benzothiazoles/benzothiazoliums (PBBs), by stretching the core structure of a prototypical fluorescent amyloid dye, thioflavin-T, with two C = C double bond inserts between aniline (or aminopyridine) and benzothiazole (or benzothiazolium) groups (Figure 1B).

All PBB compounds intensely labeled NFTs, neuropil threads, and plaque neurites in AD brains (Figure 1C). Interestingly, the affinity of these PBBs for Aβ plaques lacking dense cores was positively correlated with their lipophilicity (Figure 1C), and thereby three potential probes with relatively low logP (log of the octanol/water partition coefficient) values, including PBB3, 2-[4-(4-methylaminophenyl)-1,3-butadienyl]-benzothiazol-5,6-diol (PBB4) and PBB5 (structurally identical to Styryl 7, CAS registry number 114720-33-1), appeared suitable for visualizing tau pathologies in living organisms with reasonable selectivity. High-affinity of PBBs for tau lesions was further demonstrated by fluorometric analyses using Aβ and tau filaments assembled in a test tube (Table S1; experimental procedures are given in the Supplemental Experimental Procedures), but the most and least lipophilic PBB members displayed similar selectivity for in vitro tau versus Aβ pathologies, implying a methodological limitation in screening chemicals for tau-selective ligands based on binding to synthetic peptides and recombinant proteins. PBBs and FSB were also shown to label tau inclusions in non-AD tauopathies, such as Pick's disease (Figures 2A and S1), PSP, and CBD (Figure 2B), all of which were immunodetected by an antibody specific for phosphorylated tau proteins (AT8).

In Vitro and Ex Vivo Fluorescence Imaging of Tau Lesions in Tau Tg Mice by PBBs

To obtain in vivo evidence of direct interaction between PBBs and tau lesions, we employed Tg mice expressing a single human four-repeat tau isoform with the P301S FTDP-17 mutation (PS19 line, see Figure S2 for neuropathological features of this Tg strain) (Yoshiyama et al., 2007). Similar to the findings in non-AD tauopathy brains, NFT-like inclusions in the brain stem and spinal cord of PS19 mice were clearly recognized by PBBs (Figures 3A and S1). We then performed ex vivo labeling of tau lesions in PS19 mice with intravenously administered, fluorescently labeled PBBs. Brains and spinal cords were removed 60 min after tracer injection, and fluorescence microscopy revealed an intense accumulation of these compounds in fibrillary tau inclusions abundantly seen throughout the sections by